



**HAL**  
open science

## Efficient Gene Delivery of Tailored Amphiphilic Polypeptides by Polyplex Surfing

Paul Klemm, Jana Solomun, Marko Rodewald, Maren Kuchenbrod, Veit Hänsch, Friederike Richter, Jürgen Popp, Christian Hertweck, Stephanie Hoepfener, Colin Bonduelle, et al.

► **To cite this version:**

Paul Klemm, Jana Solomun, Marko Rodewald, Maren Kuchenbrod, Veit Hänsch, et al.. Efficient Gene Delivery of Tailored Amphiphilic Polypeptides by Polyplex Surfing. *Biomacromolecules*, 2022, 23 (11), pp.4718-4733. 10.1021/acs.biomac.2c00919 . hal-03874322

**HAL Id: hal-03874322**

**<https://hal.science/hal-03874322>**

Submitted on 29 Nov 2022

**HAL** is a multi-disciplinary open access archive for the deposit and dissemination of scientific research documents, whether they are published or not. The documents may come from teaching and research institutions in France or abroad, or from public or private research centers.

L'archive ouverte pluridisciplinaire **HAL**, est destinée au dépôt et à la diffusion de documents scientifiques de niveau recherche, publiés ou non, émanant des établissements d'enseignement et de recherche français ou étrangers, des laboratoires publics ou privés.

# Efficient Gene Delivery of Tailored Amphiphilic

## Polypeptides by Polyplex Surfing

*Paul Klemm,<sup>‡</sup> Jana I. Solomun,<sup>‡</sup> Marko Rodewald,<sup>‡</sup> Maren T. Kuchenbrod, Veit G. Hänsch,  
Friederike Richter, Jürgen Popp, Christian Hertweck, Stephanie Hoepfener, Colin Bonduelle,  
Sébastien Lecommandoux, Anja Traeger,\* Stephanie Schubert\**

Laboratory of Organic and Macromolecular Chemistry (IOMC), Friedrich Schiller University  
Jena, Humboldtstrasse 10, 07743 Jena, Germany

P. Klemm, J. I. Solomun, M. T. Kuchenbrod, F. Richter, S. Hoepfener, A. Traeger, S.  
Schubert

Leibniz Institute for Photonic Technology Jena, Member of Leibniz Health Technologies,  
Albert-Einstein-Strasse 9, 07745 Jena, Germany

M. Rodewald, J. Popp

Institute of Physical Chemistry and Abbe Center of Photonics, Friedrich Schiller University  
Jena, Lessingstrasse 10, 07743 Jena, Germany

M. Rodewald, J. Popp

Department of Biomolecular Chemistry, Leibniz Institute for Natural Product Research and  
Infection Biology, Hans Knöll Institute, Beutenbergstrasse 11a, 07745 Jena, Germany

V. G. Hänsch, C. Hertweck

Univ. Bordeaux, CNRS, Bordeaux INP, LCPO, UMR 5629, F-33600, Pessac, France

C. Bonduelle, S. Lecommandoux

21 Jena Center for Soft Matter (JCSM), Friedrich Schiller University Jena, Philosophenweg 7,

22 07743 Jena, Germany

23 P. Klemm, J. I. Solomun, M. Rodewald, M. T. Kuchenbrod, F. Richter, J. Popp, S.

24 Hoepfner, A. Traeger, S. Schubert

25 \*Correspondence: [stephanie.schubert@uni-jena.de](mailto:stephanie.schubert@uni-jena.de), [anja.traeger@uni-jena.de](mailto:anja.traeger@uni-jena.de)

26 †Paul Klemm, Jana I. Solomun and Marko Rodewald contributed equally to the study.

27

28 **ABSTRACT**

29 Within this study, an amphiphilic and potentially biodegradable polypeptide library based on  
30 poly[(4-aminobutyl)-L-glutamine-*stat*-hexyl-L-glutamine] (P(AB-L-Gln-*stat*-Hex-L-Gln)) was  
31 investigated for gene delivery. The influence of varying proportions of aliphatic and cationic  
32 side chains affecting the physicochemical properties of the polypeptides on transfection  
33 efficiency was investigated. A composition of 40 mol% Hex-L-Gln and 60 mol% AB-L-Gln  
34 (**P3**) was identified as best performer over polypeptides with higher proportions of protonatable  
35 monomers. Detailed studies of the transfection mechanism revealed strongest interaction of **P3**  
36 with cell membranes, promoting efficient endocytic cell uptake and high endosomal release.  
37 Spectrally, time-, and z-resolved fluorescence microscopy further revealed the crucial role of  
38 filopodia surfing in polyplex-cell-interaction and particle internalization in lamellipodia  
39 regions, followed by rapid particle transport into cells. This study demonstrates the great  
40 potential of polypeptides for gene delivery. Thereby, the amphiphilic character improves  
41 performance over cationic homopolypeptides, and the potential biodegradability is  
42 advantageous toward other synthetic polymeric delivery systems.

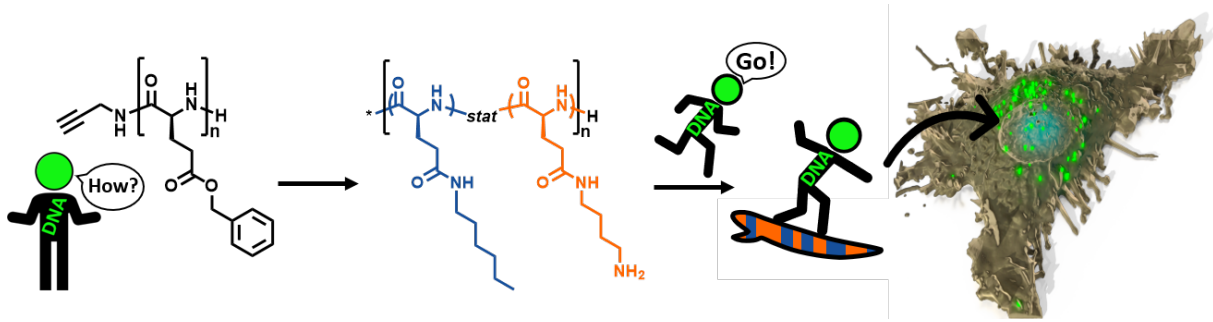
43 **KEYWORDS:** Ring opening polymerization, polypeptide, gene delivery, filopodia surfing,  
44 transfection, fluorescence microscopy

45

46

47 TOC

48



49

50

## 51 INTRODUCTION

52 Synthetic polypeptide-based materials are analogues to functional, *e.g.*, antimicrobial peptides<sup>1</sup>  
53 and a powerful tool often used in drug,<sup>2, 3</sup> and gene delivery<sup>4, 5</sup> and controlled protein release.<sup>6</sup>  
54 In particular, the development of suitable vectors for gene delivery, offering versatile  
55 possibilities for the treatment of diseases with genetic origin or for vaccination, has attracted  
56 increasing attention.<sup>7, 8</sup> To fulfill its tasks, a gene delivery vector must combine several features,  
57 *e.g.*, extracellular protection of nucleic acids from nucleases, uptake into targeted cells and  
58 sufficient release of the cargo at its site of action.<sup>9, 10</sup> Cellular uptake plays a crucial role in  
59 transfection, as one of the main barriers that must be overcome and being critical for the  
60 intracellular fate of the gene delivery vector and its cargo.<sup>11, 12</sup> To study the uptake mechanism  
61 of polyplexes, high-resolution imaging provides a powerful tool, *e.g.* to track active uptake *via*  
62 endocytosis by polyplex surfing on filopodia, which are thin membrane protrusions for  
63 scanning the cellular environment.<sup>13</sup>

64 Among non-viral gene delivery vectors, especially cationic polymers, including polypeptides,  
65 have been evaluated. One prominent example is poly(L-lysine) (PLL) as one of the first non-  
66 viral vectors, successfully complexing nucleic acids into polyplexes but revealing low  
67 transfection efficiency due to lacking endosomal escape capability.<sup>14, 15</sup> Besides protonation,  
68 also the secondary structure is a decisive factor for the delivery efficiency of polypeptides. As  
69 firstly observed for cell-penetrating peptides (CPP), an ordered  $\alpha$ -helical or  $\beta$ -sheet<sup>16</sup> secondary  
70 structure promotes cell penetration and membrane interaction, while a random coil formation  
71 as observed for PLL lacks this ability.<sup>17, 18</sup> The interaction of CPPs with cellular membranes is  
72 further enhanced by incorporation of hydrophobic moieties along the amino acid sequence  
73 creating secondary amphipathic cationic peptides with changed charge distribution, resulting in  
74 improved cellular uptake.<sup>19, 20</sup> However, these short peptides often fail to sufficiently condense  
75 and bind genetic material.<sup>21, 22</sup> Ring opening polymerization (ROP) of amino acid *N*-  
76 carboxyanhydrides (NCA) allows to generate high molar mass compounds with tailor-made

77 properties and functionalities by the choice of different monomers and initiators.<sup>5, 23, 24</sup>  
78 Furthermore, additional post modification of polypeptides is a valuable method for further fine  
79 tuning of the materials. Click chemistry is widely used in this regard as both alkenyl and azide  
80 functions are completely inert in ROP. Therefore, various strategies for introducing clickable  
81 moieties were demonstrated, such as functional monomers<sup>25, 26</sup> or the use of a suitable  
82 initiator.<sup>27</sup> Alternatively, simple starting materials like poly( $\gamma$ -benzyl-L-glutamate) (PBLG)<sup>28, 29</sup>  
83 or poly(L-glutamic acid) (PGA)<sup>30, 31</sup> can be explored for the creation of more complex  
84 structures. In this regard, post-modifications such as esterification, aminolysis and amidation  
85 are applied and allow applications of polypeptides in gene<sup>32, 33</sup> and drug delivery.<sup>34</sup> The  
86 potential of PGA has already led to a polymer-drug-conjugate, PGA-paclitaxel (CT-2103)  
87 [XYOTAX], which is currently in clinical trials for cancer therapy.<sup>35, 36</sup> So far, for gene  
88 delivery, mainly cationic homopolypeptides with ordered secondary structures have been  
89 investigated, showing improved efficiency compared to their random coil counterparts,<sup>37, 38</sup> and  
90 only few studies explored the potential of amphiphilic polypeptides in transfection.<sup>39-41</sup>  
91 In this study, we now combine the beneficial properties, *i.e.*, an ordered secondary structure  
92 and a tailored cationic/hydrophobic balance, for the design of synthetic polypeptides for gene  
93 delivery. We present a small library of synthetic amphiphilic polypeptides **P1** to **P5** based on  
94 poly[(4-aminobutyl)-L-glutamine-*stat*-hexyl-L-glutamine] (P(AB-L-Gln-*stat*-Hex-L-Gln)). The  
95 amphiphilic polypeptides were prepared *via* a four-step synthetic route, characterized in terms  
96 of their physicochemical properties depending on the ratio of AB-L-Gln- and Hex-L-Gln,  
97 formulated into DNA polyplexes and screened for their gene delivery potential. Here, the  
98 amphiphilic polypeptide **P3**, which has a high proportion of hydrophobic side chains and  
99 ordered secondary structures but still remains soluble in aqueous buffers, showed the highest  
100 efficiency. To gain insight into the transfection mechanism and the influence of the  
101 cationic/hydrophobic balance on membrane interactions, endosomal release ability and cellular  
102 uptake were studied. For an even deeper understanding of the polyplex acquisition, the transport

103 and the internalization process by the cells, spectrally, time- and z-resolved fluorescence  
104 microscopy of live and fixed cells and complementary transmission electron microscopy were  
105 employed. Thereby, an filopodia and lamellipodia-based initial acquisition mechanism of the  
106 amphiphilic polypeptides was identified, which is followed by cellular internalization. Overall,  
107 this study highlights the importance of the cationic/hydrophobic balance of amphiphilic  
108 polypeptides for transfection efficiency and further reveals the mechanism of the so far  
109 underestimated and unstudied step of initial acquisition of amphiphilic polypeptides by  
110 lamellipodia and filopodia. These findings are thus giving essential insights for the further  
111 design of tailor-made polypeptides for efficient gene delivery.

## 112 **EXPERIMENTAL**

113 **Ring opening polymerization of BLG-NCA.** In a glovebox filled with argon, BLG-NCA  
114 (12 g, 45.68 mmol) was added to a fire-dried Schlenk flask and dissolved in 48 mL  
115 dimethylformamide (DMF,  $c_M = 0.95$  M). For the initiator stock solution, 200  $\mu$ L propargyl  
116 amine (3.12 mmol) were diluted in 1 mL anhydrous DMF ( $c = 2.60$  M). The polymerization  
117 was initiated by adding 175  $\mu$ L of the initiator stock solution (monomer to initiator ratio  
118 (M/I) = 100) to the highly agitated reaction solution. The solution was stirred overnight at room  
119 temperature (RT) under inert atmosphere. The conversion of the monomer was followed by  
120 infrared (IR) measurements (Figure S1). The resulting solution was precipitated in a large  
121 excess of diethyl ether. The solid was separated by centrifugation (2132 g, 4 °C, 4 min) and  
122 washed three times with 30 mL diethyl ether. All supernatants were discarded. A colorless  
123 powder was obtained by freeze-drying. Yield: 8.88 g (88 %). The polymer was characterized  
124 by proton nuclear magnetic resonance ( $^1\text{H-NMR}$ ) spectroscopy in deuterated trifluoroacetic  
125 acid (d-TFA) including traces of deuterated chloroform ( $\text{CDCl}_3$ , Figure S2B), size exclusion  
126 chromatography (SEC) in dimethylacetamide (DMAc) containing 0.21 wt% LiCl (Figure S3A),  
127 IR (Figure S4) and Raman spectroscopy (Figure S5).

128



129 **PGA synthesis via ester hydrolysis of PBLG side chains.** PGA was synthesized according to  
130 a known procedure.<sup>42</sup> To a solution of PBLG (3 g, 15.43 mmol BLG units) in 22.5 mL TFA,  
131 3.4 mL HBr (48 %, 62.61 mmol, 4 eq. per BLG unit) were added dropwise. The solution was  
132 stirred for 18 h at RT. The reaction mixture was precipitated in a large excess of diethyl ether.  
133 The precipitant was separated by centrifugation (2132 g, 4 °C, 4 min) and washed three times  
134 with diethyl ether. All supernatants were discarded. A colorless powder was obtained by freeze-  
135 drying. Yield: 1.66 g (92 %). The product was characterized by <sup>1</sup>H-NMR spectroscopy in d-  
136 TFA including traces of CDCl<sub>3</sub> (Figure S2A), by SEC in 0.08 M Na<sub>2</sub>HPO<sub>4</sub>/0.05 % NaN<sub>3</sub>  
137 (pH = 9) solution as eluent (Figure S3B), by IR (Figure S4) and Raman spectroscopy (Figure  
138 S5), and by elemental analysis (found: Br 1.79 %).

139  
140 **General procedure of 1-Ethyl-3-(3-dimethylaminopropyl)carbodiimide (EDC) coupling**  
141 **of *n*-hexylamine (HexA) and *N*-(*tert*-butoxycarbonyl)-1,4-diaminobutylamine (BocDAB)**  
142 **with PGA.** The detailed amounts of the reactants are summarized in Table S2. PGA was  
143 dissolved in DMF (c = 0.47 M). Successively, hydroxybenzotriazole monohydrate (HOBT),  
144 1.5 eq. per L-Glu unit), HexA (1.10 - 0.31 eq. per L-Glu unit) and BocDAB (0.5 - 0.1 eq. per L-  
145 Glu unit) were added and the reaction mixture was stirred for 10 min. EDC (1.50 eq. per L-Glu  
146 unit) was added to the resulting suspension and stirred for 18 h at RT. The reaction mixture was  
147 precipitated in a large excess of diethyl ether. The solids were separated by centrifugation  
148 (2132 g, 4 °C, 4 min) and washed 3 times with diethyl ether. All supernatants were discarded.  
149 After drying under reduced pressure, the residue was washed three times with water. A colorless  
150 powder was obtained by freeze-drying. The product was characterized by <sup>1</sup>H-NMR  
151 spectroscopy in d-TFA including traces of CDCl<sub>3</sub> (Figure 1) and by SEC in DMAc containing  
152 0.21 wt% LiCl (Figure S3A) as well as by IR spectroscopy (Figure S7). The respective amount  
153 of BocDAB or HexA (mol% and degree of polymerization (DP)) in each compound,  
154 summarized in Table 1, was calculated by area correlation of the characteristic signals in the

155 <sup>1</sup>H-NMR spectra using the Peak Analyzer of Origin 9.1.0G (© by OriginLab Corporation),  
156 according to a procedure published elsewhere, Figure S8.<sup>5</sup> In addition, the DP of PBLG was  
157 presumed as total DP of **PP1 - PP4** and **P5**. The theoretical molar mass ( $M_{n,theo}$ ) was calculated  
158 by adding the molar mass of all 96 units and of the initiator.

159

160 **General procedure of Boc deprotection (P1 to P4).** The detailed amounts of the reactants are  
161 summarized in Table S3. In a reaction vessel, poly[(4-(N-tert-butoxycarbonylaminobutyl)-L-  
162 glutamine-*stat*-hexyl-L-glutamine] (P(BocAB-L-Gln-*stat*-Hex-L-Gln)) (250 mg) was dissolved  
163 in 2.5 mL TFA and stirred overnight at RT. Then, the pH value of the reaction solution was  
164 adjusted to 7.4 using a saturated solution of NaHCO<sub>3</sub>. The resulting mixture was dialyzed  
165 against water with a regenerated cellulose membrane (MWCO 3.5 kDa, SpectraPor RC, Carl  
166 Roth) with regular water changes to remove all salt impurities. A colorless powder was obtained  
167 by freeze-drying. The product was characterized by <sup>1</sup>H-NMR spectroscopy in d-TFA including  
168 traces of CDCl<sub>3</sub> (Figure S9), Raman- (Figure S5) and CD spectroscopy (Figure 1B).

169

170 **Polyplex formulation.** pDNA-loaded polyplexes were formulated either in phosphate buffered  
171 saline solution (PBS) or 4-(2-hydroxyethyl)-1-piperazineethanesulfonic acid) (HEPES)  
172 buffered glucose solution (HBG, 5 % (w/v) glucose, 20 mM HEPES, pH 7.4). Therefore, stock  
173 solutions of the polypeptides in PBS or 0.2 M sodium acetate buffer (pH 5.8) were diluted with  
174 PBS (PBS polyplex) or HBG buffer (HBG polyplex), respectively. To obtain a nitrogen to  
175 phosphate (N/P) ratio of 5 and 10, the polymers were mixed with pDNA dissolved in ultrapure  
176 water at a volume ratio of 1:2 followed by vortexing for 10 s. The samples were incubated for  
177 15 min at RT prior to usage.

178

179 **Cell culture.** The mouse fibroblast cell line L-929 was cultured in Dulbecco's modified eagle  
180 medium (DMEM, 1 g L<sup>-1</sup> glucose), supplemented with 10 % (v/v) fetal bovine serum (FBS),

181 100U mL<sup>-1</sup> penicillin, 100 µg mL<sup>-1</sup> streptomycin (D10) at 37 °C in a humidified 5 % (v/v) CO<sub>2</sub>  
182 atmosphere.

183

184 **Transfection of L-929 Cells.** For transfection experiments, L-929 cells were seeded in a 48-  
185 well format at a density of  $0.1 \times 10^6$  cells mL<sup>-1</sup> in 250 µL D10 per well and incubated for 24 h.  
186 The medium was changed to 225 µL fresh D10 1 h prior to treatment. Polyplexes were prepared  
187 as described above using DH-pEGFP-N1 pDNA. pKMyC pDNA (not encoding for green  
188 fluorescent protein) was used as negative control. The polyplexes were prepared at N/P ratios  
189 of 5 and 10 and final pDNA concentrations of 3 and 4.5 µg mL<sup>-1</sup> per well. The cells were treated  
190 with 25 µL of the samples or respective buffer as control and incubated with the samples for  
191 24 h. Subsequently the cells were detached by trypsin-ethylenediaminetetraacetate (trypsin-  
192 EDTA), resuspended in Hanks' balanced salt solution (HBSS) buffer (supplemented with 2 %  
193 FBS and 20 mM HEPES) and measured *via* flow cytometry ( $\lambda_{\text{EX}} = 488$  nm combined with a  
194 525/40 nm bandpass filter, FITC channel). Viable single cells expressing green fluorescence  
195 protein (GFP) were identified by gating to the negative control (polyplex with pKMyC pDNA).  
196 The gating strategy is shown in detail in Figure S10. Cells were further imaged by fluorescence  
197 microscopy using brightfield imaging and the FITC channel ( $\lambda_{\text{EX}} = 469/35$  nm,  
198  $\lambda_{\text{EM}} = 525/39$  nm) <sup>43</sup>.

199

200 **Endosomal escape *via* calcein release assay.** For investigations of endosomal escape, a calcein  
201 assay was performed as previously described with slight adaptations of the procedure.<sup>44, 45</sup> L-929  
202 cells were seeded in 24-well ibiTreat plates at a density of  $0.1 \times 10^6$  cells mL<sup>-1</sup> in 500 µL D10  
203 and incubated for 24 h. The medium was changed to fresh D10 1 h prior to treatment.  
204 Polyplexes were prepared as described above (N/P 10, 4.5 µg mL<sup>-1</sup> pDNA per well). For  
205 treatment, 10 µL calcein (2.5 mg mL<sup>-1</sup>) were added per well to give a final concentration of  
206 50 µg mL<sup>-1</sup>, directly followed by 50 µL of the samples. Following 1 h of incubation, the cells

207 were washed twice with warm FC buffer and 500  $\mu$ L warm D20 (DMEM supplemented with  
208 20 % FBS) was added. The cells were subsequently stained with 8  $\mu$ M Hoechst 33342 and  
209 imaged *via* confocal laser light scanning microscopy (CLSM). Calcein was excited at 488 nm  
210 by applying the argon laser (1 %) using emission filters for 490–544 nm. For excitation of  
211 Hoechst, the Argon laser at 405 nm (0.5 %) was used with a detection filter for 410–469 nm.  
212 To avoid cross talk, calcein and Hoechst were imaged in two separate tracks using the frame  
213 scan modus. Images were acquired using the ZEN software, version 2.3 SP1 (Zeiss) and were  
214 processed using ImageJ (Version 1.52a, National Institutes of Health).<sup>46</sup> Image analysis for  
215 quantification of cells with released calcein, was conducted as described before, with slight  
216 adjustments of image processing steps and is described in detail in the SI <sup>45</sup>.

217

218 **Cellular uptake of the polyplexes in L-929 cells measured *via* flow cytometry.** To study  
219 cellular uptake *via* flow cytometry, L-929 cells were seeded in a 48-well format as described  
220 for transfection experiments. The medium was changed to 225  $\mu$ L fresh D10 1 h prior to  
221 treatment. For polyplex preparation (N/P 5 and 10, 1.5  $\mu$ g mL<sup>-1</sup> pDNA), pKMyC pDNA was  
222 labeled with YOYO-1 iodide (0.027 nmol per 1  $\mu$ g pDNA) and subsequently mixed with the  
223 polypeptides as described above. In the following, the assay was performed as described  
224 before.<sup>44</sup> Briefly, 25  $\mu$ L of the samples were added per well and the cells were incubated with  
225 the samples for 1 h, 4 h and 24 h. Subsequently, the cells were detached and resuspended as  
226 described for transfection experiments and Trypan Blue solution was added at a concentration  
227 of 0.04 % per well. Additionally, the cells were stained once with propidium iodide (PI) to gate  
228 the viable cells. PI was added to a final concentration of 1  $\mu$ g mL<sup>-1</sup>, and the cells were then  
229 measured *via* flow cytometry ( $\lambda_{\text{EX}}$  = 488 nm, 610/20 nm bandpass filter). PI-negative cells were  
230 gated according to the positive control linear poly(ethyleneimine) (LPEI) without pDNA, final  
231 concentration of 100  $\mu$ g mL<sup>-1</sup>) and negative control (PBS buffer). YOYO-1 fluorescence was  
232 measured using the FITC channel. Viable single cells showing increased YOYO-1 fluorescence

233 intensity (FI) were identified by gating to the negative control (pDNA labeled with YOYO-1)  
234 and the relative mean fluorescence intensity (rMFI) of all viable single cells was calculated  
235 relative to the negative control. A detailed gating strategy is shown in the SI (Figure S11).

236

### 237 **Cellular uptake of P2 and P3 polyplexes in L-929 cells imaged by fluorescence microscopy.**

238 To monitor cellular uptake *via* fluorescence microscopy, L-929 cells were seeded into 4-well  
239 glass bottom dishes (Greiner) at a density of  $0.2 \times 10^6$  cells mL<sup>-1</sup> in 500 μL D10 and incubated  
240 for 24 h. Polyplexes of **P2** (N/P 5) and **P3** (N/P 10) were prepared using pKMyC pDNA, which  
241 was labeled with YOYO-1 as described above at a final pDNA concentration of 1.5 μg mL<sup>-1</sup>  
242 per well. For live cell imaging, the cells were stained with CellMask™ Deep Red membrane  
243 stain (CMDR), Thermo Fisher Scientific, 1× working solution in HBSS buffer prepared from  
244 1000x concentrated stain solution). For staining, the supernatant was removed, the cells were  
245 washed once with 500 μL PBS buffer, and 100 μL of the staining solution was added per well.  
246 After 8 min of incubation, the staining solution was removed, and the cells were washed three  
247 times with PBS buffer, followed by addition of 250 μL fresh D10 per well. For treatment, 50 μL  
248 of the polyplex solution was diluted with 200 μL D10 and added to the cells to obtain a final  
249 volume of 500 μL per well. After incubation and live cell imaging (100 min), the cells were  
250 washed three times with PBS, and cells treated with **P3** polyplex were fixed with 4 %  
251 paraformaldehyde (PFA) solution in water by 10 min incubation at 37 °C. The cells were then  
252 washed three times with PBS, 500 μL PBS was added per well and the cells were stored in the  
253 fridge overnight before z-resolved measurements. For measurements of fixed cells treated with  
254 **P2** polyplex, the medium was changed to 450 μL fresh D10 1 h prior to treatment.  
255 Subsequently, 50 μL of **P2** polyplex solution was added per well and incubated with the cells  
256 for 15 min, followed by CMDR staining and fixation with PFA as described above, and  
257 immediate transfer to the microscope.

258 Two-channel images (CMDR, YOYO-1) were recorded using simultaneous excitation (488 nm  
259 (YOYO-1), 650 nm (CMDR); white light laser, Leica) and the internal monochromators. For  
260 all data, except the spectrally resolved YOYO-1 data, the signals were detected in the spectral  
261 ranges 503 - 628 nm and 665 - 800 nm, respectively. For spectrally resolved YOYO-1 data, the  
262 excitation wavelength was set to 483 nm and detection was performed in increments of 5 nm  
263 and with detection windows of 5 nm. The pinhole for confocal operation was opened to account  
264 for 1 airy disk in all measurements. Detailed parameters for every measurement are part of the  
265 SI.

266

267 **Sample preparation for imaging of cellular uptake of P2 and P3 polyplexes in L-929 cells**  
268 **by transmission electron microscopy (TEM).** For uptake studies *via* TEM, L-929 cells were  
269 seeded into 6-well cell culture plates at a density of  $0.5 \times 10^6$  cells mL<sup>-1</sup> in 2 mL D10 and  
270 incubated for 24 h. Medium was changed to 1.8 mL fresh D10 1 h prior to treatment. Polyplexes  
271 of **P2** (N/P 5) and **P3** (N/P 10) were prepared using pKMyC pDNA at a final pDNA  
272 concentration of 4.5 µg mL<sup>-1</sup> per well and 200 µL of the sample was added per well. After  
273 incubation for 1 h, the cells were detached by trypsin-EDTA and resuspended in 450 µL D10.  
274 For embedding, the cells were washed three times with PBS and centrifuged at 100 g for  
275 2 min.<sup>47</sup> The cells were fixated on ice for 1 h in an 2.5 % glutaryl aldehyde, 1 % osmium  
276 tetroxide PBS solution. To remove any residues, the fixed cells were subsequently washed twice  
277 for 15 min with PBS. Dehydration of the cells was reached by replacing the buffer solution  
278 stepwise (50 %, 70 %, 90 %, 100 %) with ethanol (EtOH). 18 µL 2,4,6-  
279 tri(dimethylaminomethyl) phenol solution (DMP-30) were added per mL to a previously  
280 prepared Embed812 (EMbed 812, dodecyl succinic anhydride (DDSA) and methyl-5-  
281 norbornene-2,3-dicarboxylic anhydride (NMA) in the ratio 1:1.1:0.25) solution. In a first step,  
282 the embedding solution was added to the cells for 1 h with a ratio of 2:1 with EtOH.  
283 Subsequently, the cells were centrifuged at 100 g for 8 min and the residual embedding solution

284 was removed followed by adding pure Embed812/DMP-30 solution, incubation at RT  
285 overnight and centrifugation again. After the removal of the residual embedding solution,  
286 freshly prepared Embed812/DMP-30 solution was added and incubated for 2 h at RT.  
287 Afterwards the cells were transferred to BEEM® capsules and centrifuged again. Residual  
288 embedding solution was removed before fresh Embed812/DMP-30 solution was added, and the  
289 samples were dried at 60 °C overnight in the drying oven. The dried sample was cut in 100 nm  
290 slices. Each slice was stained with 4 % uranyl acetate solution for 20 min and subsequently  
291 with lead citrate for 5 min. The slices were transferred onto Quantifoil® carbon supported film  
292 grids (Cu 300 mesh) and subjected to TEM measurements. For cryo-TEM investigations, 9 µL  
293 of the particle solutions were deposited on a Quantifoil grid (R2/2) in a Vitrobot Mark IV.  
294 Samples were blotted at a blot force of -1 for 1 s and rapidly immersed into liquid ethane serving  
295 as the cryogen. Grids were transferred into the cryo-holder (Gatan 626) utilizing the Gatan cryo  
296 transfer stage. During the entire process after vitrification in ethane, the temperature was  
297 maintained at temperatures lower than 175 °C. Images were acquired on a side-entry CCD  
298 camera (MegaView, Olympus Soft Imaging Solutions).

299

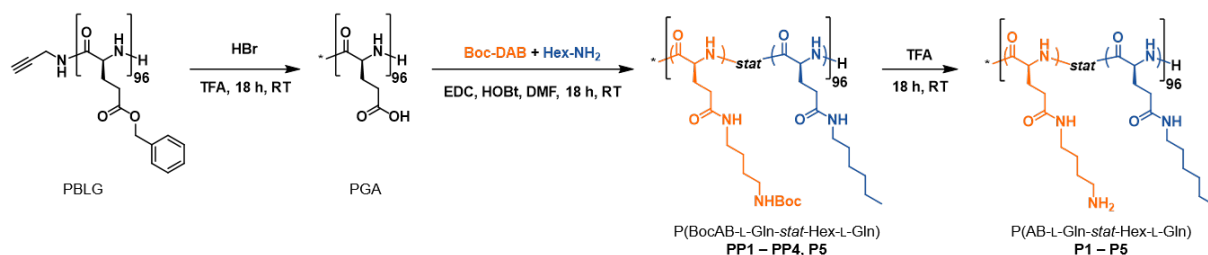
300 **Statistical analysis.** Statistically significant differences within transfection and uptake  
301 experiments measured by flow cytometry were determined by analyzing multiple groups by  
302 two-way mixed analysis of variance (two-way mixed ANOVA) and a Bonferroni's post-hoc  
303 test. Statistical significance is indicated as follows: \*/#  $p < 0.05$ , \*\*/##  $p < 0.01$ , and \*\*\*/###  
304  $p < 0.001$  and analysis was conducted using OriginPro2021 software.

305

## 306 **RESULTS AND DISCUSSION**

307 **Polymer synthesis and characterization.** Cationic functionalities are necessary to enable the  
308 complexation of pDNA and the formation of a polyplex. Therefore, a small library consisting  
309 of the pure polycation P(AB-L-Gln) P1, the amphiphilic polypeptides P(AB-L-Gln-*stat*-Hex-L-

310 Gln) P2 - P4 and the hydrophobic P(Hex-L-Gln) P5 were prepared at room temperature (RT)  
 311 by amidation of PGA and deprotection of the Boc-AB-L-Gln units of the protected polymers  
 312 (PP1 - PP4), Scheme 1. PGA was obtained by classical ester hydrolysis of the starting material  
 313 PBLG <sup>42</sup>.



314  
 315 **Scheme 1:** Schematic representation of the synthesis route of P(AB-L-Gln-*stat*-Hex-L-Gln) **P1**  
 316 (100 mol% AB-L-Gln : 0 mol% Hex-L-Gln), **P2** (84 mol% : 16 mol%), **P3** (60 mol% :  
 317 40 mol%), **P4** (30 mol% : 70 mol%) and **P5** (0 mol% : 100 mol%).

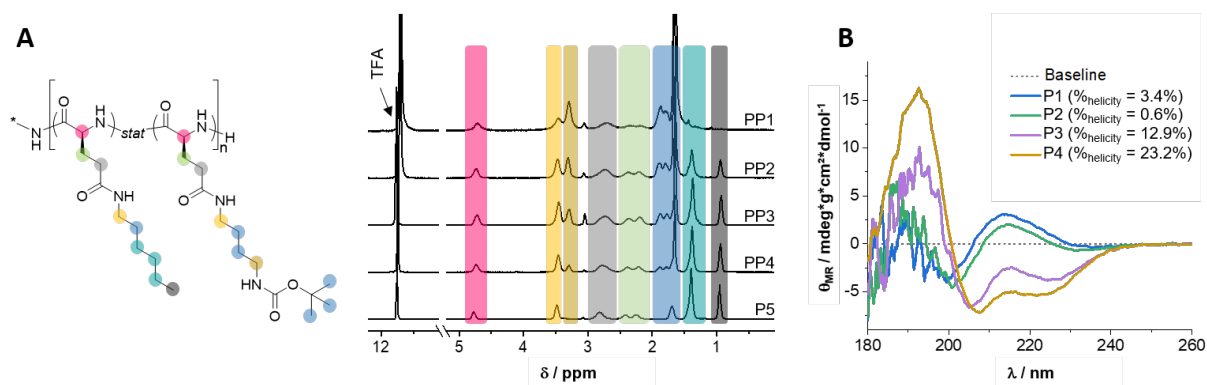
318 PBLG was synthesized *via* ROP from BLG-NCA. Propargyl amine was used as an initiator  
 319 with a M/I of 100 to allow a simplified determination of the DP based on the isolated signal in  
 320 the <sup>1</sup>H-NMR of the methylene protons at  $\delta = 4.07$  ppm (Figure S2). The conversion of the  
 321 monomer was monitored by IR spectroscopy. After four days, the complete disappearance of  
 322 the characteristic NCA bands at  $\tilde{\nu} = 1853$  cm<sup>-1</sup> and  $1786$  cm<sup>-1</sup> indicated complete conversion  
 323 (Figure S1). PBLG is narrowly distributed with a polydispersity index ( $\mathcal{D}$ ) of 1.07 as determined  
 324 by SEC (Figure S3, Table S1). Using the <sup>1</sup>H-NMR spectrum in Figure S2, a chain length of on  
 325 average 96 monomer units was obtained by integrating the signal from the chiral proton in the  
 326 polymer backbone at  $\delta = 4.76$  ppm, relative to the two protons of the methylene group of the  
 327 starting group at  $\delta = 4.07$  ppm. Starting from PBLG, three modification steps were required to  
 328 reach the targeted structures **P1** to **P4** (Scheme 1).

329 The cleavage of the benzyl ester of PBLG led to PGA. The Raman spectra of both compounds  
 330 (Figure S5) show the complete disappearance of the aromatic CH stretching vibration at  
 331  $\tilde{\nu} = 3065$  cm<sup>-1</sup>, as well as the aromatic ring breathing mode at  $\tilde{\nu} = 1004$  cm<sup>-1</sup> and the  
 332 accompanying peak at  $\tilde{\nu} = 1031$  cm<sup>-1</sup>, which is typical for mono-substituted aromatic  
 333 compounds and, thus, indicates complete conversion. Accordingly, IR spectra of PGA (Figure



334 S4) show the presence of carboxylic OH groups at  $\tilde{\nu} \sim 1700 \text{ cm}^{-1}$  and the signal at  
335  $\tilde{\nu} \sim 3300 \text{ cm}^{-1}$ , which is partially obstructed by the broad NH stretching mode. The  
336 disappearance of all benzylic protons in the  $^1\text{H-NMR}$  spectra (Figure S2) further confirms the  
337 successful hydrolysis of the ester side arms. Elemental analysis of PGA showed 1.79 % Br,  
338 indicating the presence of some hydrobromides and potentially a partial HBr addition to the  
339 triple bond. However, stoichiometric conversion with 2 eq. HBr could only account for 1.26 %  
340 Br, and all intermediates (**PP1 - PP4**) and final products (**P1 - P5**) show the characteristic  
341 resonance of  $\text{C}\equiv\text{C}$  triple bonds at  $2130 \text{ cm}^{-1}$  in their Raman spectra (Figure S5), indicating that  
342 addition of HBr in the first reaction step is a minor concern. Because of the lack of suitable,  
343 *i.e.*, non-overlapping and constant peaks in  $^1\text{H-NMR}$ , quantitative statements about the DP of  
344 PGA are difficult to make. SEC measurements of PGA (Figure S3B) show a tailing that can be  
345 explained by interactions with the column. The high molar mass ( $M_n$ ) and  $D$  of PGA compared  
346 to PBLG as determined by SEC can be explained by the aqueous eluent and a different  
347 calibration (Table S1).

348 After ester hydrolysis, the carboxylic acid functionalities were now available to couple amines  
349 in various ratios by activation with EDC and HOBt activation. Therefore, the mono-protected  
350 compound of DAB, *i.e.*, BocDAB, was used to prevent crosslinking when working with dual-  
351 functional DAB. In addition, hydrophobic HexA was chosen to lower the toxicity of the  
352 polycation while ensuring efficient complexation of pDNA and preventing random coil  
353 formation as secondary structures. To investigate the changes in chemical, structural,  
354 spectroscopic, and biological behaviors, two homopolymers (**PP1** and **P5**) and three  
355 copolymers (**PP2 - PP4**) with different ratios of HexA and BocDAB were synthesized, Table  
356 S2. **PP2** and **PP3** were synthesized with an excess of BocDAB compared to HexA, while a  
357 substoichiometric amount of BocDAB was used for **PP4**. Figure 1 shows the  $^1\text{H-NMR}$  spectra  
358 of **PP1** to **PP4** and **P5**. The detection of the starting group is shown in Figure S12.



359

360 **Figure 1** A  $^1\text{H-NMR}$  spectra of **PP1** to **PP4** and **P5** measured at 25 °C and 300 MHz in  
 361 deuterated d-TFA containing traces of  $\text{CDCl}_3$ . **B** Overlay circular dichroism (CD) spectra of  
 362 **P1** – **P4** measured in 1,1,1,3,3,3-hexafluoro-2-propanol (HFIP) ( $c_{\text{pi}} = 0.50 \text{ mg mL}^{-1}$ ). Mean  
 363 residual ellipticity  $\theta_{\text{MR}}$  calculated with Equation S6 including  $\%_{\text{helicity}}$  calculated with Equation  
 364 S7.

365

366 Both, ester hydrolysis and EDC coupling do not change the total DP of 96, which was  
 367 determined for PBLG and, thus, also applies to the intermediates. The content of BocDAB and  
 368 HexA can be determined by correlating the characteristic signals of both moieties in their  $^1\text{H-}$   
 369 NMR spectrum.<sup>5</sup>  $^1\text{H-NMR}$  studies revealed the following ratios of BocAB-L-Gln and Hex-L-  
 370 Gln: **PP1** 100 mol%:0 mol%, **PP2** 84 mol%:16 mol%, **PP3** 60 mol%:40 mol%, **PP4**  
 371 30 mol%:70 mol% and **P5** 0 mol%:100 mol%, Table 1. The elugrams of **PP1** to **PP4** measured  
 372 by SEC showed monomodal distributions in all cases with low  $D$  around 1.17 (Figure S3A). **P5**  
 373 is insoluble in all common solvents except TFA, consequently, investigation with the given  
 374 SEC systems was not possible. The  $M_n$  values determined by universal PS calibration are  
 375 comparable to  $M_{n,\text{theo}}$  calculated from the  $^1\text{H-NMR}$  results, Table 1. The cleavage of the Boc  
 376 protecting group from **PP1** to **PP4** in pure TFA resulted in **P1** to **P4**. The disappearance of the  
 377 prominent singlet at  $\delta = 1.6 \text{ ppm}$  in  $^1\text{H-NMR}$  spectroscopy (Figure S9A) indicates a complete  
 378 deprotection of the amines of **PP1** to **PP4**. The SEC studies in Figure S9B show that polymers  
 379 **P1**, **P2** and **P3** are still intact. However, in the case of **P3**, a second population elutes with a  
 380 lower elution volume, indicating a higher molar mass species. This could be caused by  
 381 interactions of the polymer with the stationary phase of column material or by self-assembly of

382 the polymer in the eluent. SEC analysis was not possible for **P4** and **P5** due to their insolubility  
 383 in the eluent used.

384 **Table 1:** Results of analytical investigations of **PP1** to **PP4** and **P5**.

	<sup>1</sup> H-NMR <sup>a)</sup>					SEC <sup>b)</sup>		Yield	ID
	M <sub>n,theo</sub>	mol% <sub>BocAB</sub>	DP	mol% <sub>Hex</sub>	DP	M <sub>n</sub>	Đ		
	kg mol <sup>-1</sup>					kg mol <sup>-1</sup>		%	
<b>PP1</b>	28.8	100	96	-	-	24.0	1.15	62	<b>P1</b>
<b>PP2</b>	27.5	84	81	16	15	24.7	1.13	51	<b>P2</b>
<b>PP3</b>	25.5	60	58	40	38	23.0	1.17	71	<b>P3</b>
<b>PP4</b>	22.9	30	29	70	67	21.5	1.21	68	<b>P4</b>
<b>P5</b>	20.4	-	-	100	96	-	-	69	<b>P5</b>

385 a) <sup>1</sup>H-NMR measured in d-TFA containing traces of CDCl<sub>3</sub> at 25 °C and 300 MHz. In each  
 386 case, sum of DP<sub>BocAB</sub> and DP<sub>Hex</sub> gives a total DP of 96 (DP of PBLG). b) SEC  
 387 measurements were determined by using DMAc/0.21 wt% LiCl as eluent, RI detector and a  
 388 polystyrene (PS) calibration.

389

390 **Investigation of the secondary structures.** Previous studies have already shown that the  
 391 secondary structure of a polypeptide has an impact on effective cell uptake through  
 392 destabilization of the membrane.<sup>48</sup> In Figure S13A, IR spectra of solid **P1** to **P5** show the  
 393 influence of the aliphatic side arms. With increasing content of HexA, the band of β-sheets also  
 394 increased at  $\tilde{\nu}_\beta \sim 1625 \text{ cm}^{-1}$ , while the band for α-helices decreases at  $\tilde{\nu}_\alpha \sim 1645 \text{ cm}^{-1}$ . In  
 395 addition, it can be suspected that less amount of random coil structures was formed  
 396 ( $\tilde{\nu}_{\text{rc}} \sim 1650 \text{ cm}^{-1}$  and  $\tilde{\nu}_{\text{rc}} \sim 1538 \text{ cm}^{-1}$ ) with an increasing content of HexA. Therefore, in solid  
 397 state, it can be assumed that at the transition from **P2** to **P4** the content of α-helices and β-sheets  
 398 exceeds that of random coil formation. Merely the spectra of **P1** complicates the interpretation  
 399 of the macrostructure of the compound. However, the shape of the curve may indicate  
 400 overlapping bands of α-helices, β-sheets, and random coil formations. Therefore, it can be  
 401 assumed that **P1** has the highest content of random coil formation compared to the other

402 compounds probably due to its purely cationic structure. To confirm the results of the solid-  
403 state IR studies, CD measurements were performed on polymers **P1** to **P4** dissolved in HFIP, a  
404 solvent suitable for CD spectroscopy.<sup>49</sup> The curves of **P1** and **P2** show the characteristic shape  
405 of coil formation with a maximum at 215 nm (Figure 1B).<sup>50</sup> In contrast, polymers **P3** and **P4**  
406 show two minima at 205 and 222 nm, which can be assigned to  $\alpha$ -helix formation. In addition,  
407 CD measurements were performed with polyplexes of **P1** to **P3** dissolved in phosphate buffered  
408 saline (PBS, pH 7.4) (N/P 10), Figure S13B. Due to their insolubility, **P4** and **P5** were not  
409 suitable for polyplex formulation. The results derived from the profiles of **P1**, **P2** and **P3** in  
410 physiological environment are comparable to their behavior dissolved in HFIP. The spectra of  
411 the polyplexes of **P1** indicate mainly random coil formation, whereas the shape of **P2** reveals a  
412 mixture of random coil and  $\alpha$ -helix formation.<sup>51</sup> The curve of the polyplexes of **P3** suggest a  
413 mixture of  $\beta$ -sheet and  $\alpha$ -helix formation.

414

415 **DNA binding and release.** To utilize the synthesized polypeptides as gene delivery vectors,  
416 their pDNA binding and release capability was evaluated. First, the polypeptides were dissolved  
417 in PBS (pH 7.4) or acetate buffer (0.2 M, pH 5.8) to test their solubility. **P1** and **P2** were highly  
418 soluble in both buffers, while **P3** showed lower solubility in PBS. **P4** with the highest content  
419 of hydrophobic HexA groups was not soluble in both buffers and was, therefore, excluded from  
420 the study. pDNA binding was measured using the ethidium bromide binding assay (EBA).  
421 Therefore, polyplexes were prepared with ethidium bromide (EtBr) labelled pDNA in PBS  
422 (PBS polyplex) or a mixture of acetate buffer and HBG buffer (HBG polyplex) at various N/P  
423 ratios (1 to 30), followed by monitoring of EtBr fluorescence (Figure S14A). All investigated  
424 polypeptides showed pDNA binding at  $N/P > 1$  independent of the buffer system used, as  
425 indicated by the plateau reached in relative fluorescence intensity (rFI). These results clearly  
426 show that for all polymers the N/P ratio and thus the total amount of primary amino groups  
427 (AB-L-Gln) is the decisive factor for pDNA condensation, independent of the molar ratio of

428 AB-L-Gln and hydrophobic Hex-L-Gln within the statistical polymers. Differences were  
429 observed in the level of the plateaus, with rFI decreasing to ~ 50 % for PBS and ~ 10 % for  
430 HBG polyplexes, indicating a stronger binding in HBG. In comparison, PBS polyplexes might  
431 be less charged either due to higher pH values or shielding of amine groups by phosphate ions  
432 present in the solution. Nevertheless, in both buffer formulations all polypeptides (**P1 - P3**)  
433 successfully bind pDNA at N/P ratios  $\geq 5$ . As pDNA further needs to be released within the  
434 cell for successful gene delivery, dissociation of the polyplexes in the presence of heparin as  
435 competing anion was studied by monitoring EtBr fluorescence upon addition of increasing  
436 amounts of heparin (Figure S14B). All polyplexes showed pDNA release at heparin  
437 concentrations above  $9 \text{ U mL}^{-1}$ . HBG polyplexes of all polypeptides completely released  
438 pDNA at  $20 \text{ U mL}^{-1}$ . Release efficiencies in PBS showed the same tendencies but did not reach  
439 100 % release in all cases. These results further support the assumption of pronounced  
440 hydrophobic interactions in PBS, being less prone to displacement by highly negatively charged  
441 heparin.<sup>52, 53</sup> Overall, the polypeptides **P1** to **P3** showed good pDNA binding and release and  
442 are therefore suitable candidates for gene delivery.

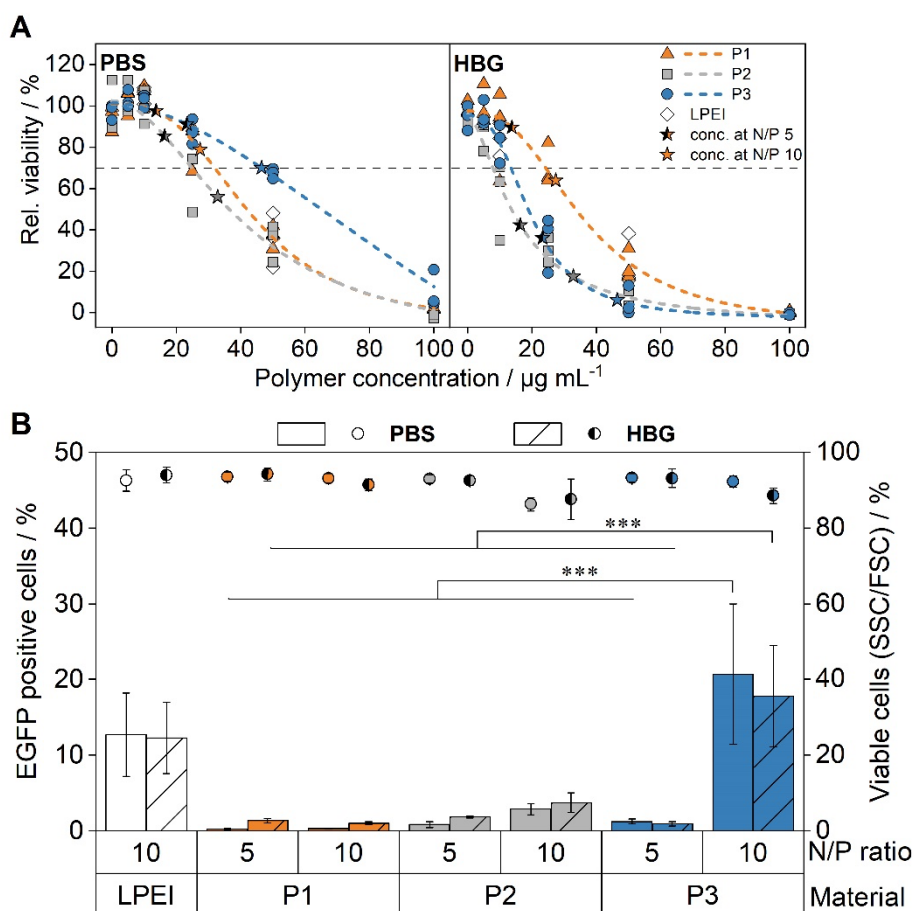
443 **Toxicity and transfection efficiency in L-929 cells.** A PrestoBlue™ assay was performed in  
444 L-929 cells by incubating the cells with the polymers dissolved in PBS or acetate/HBG buffer  
445 to evaluate their toxicity (Figure 2A). The L-929 cell line was chosen as standard cell line for  
446 cytotoxicity testing recommended by the ISO 10993-5 guideline. Further, this cell line has been  
447 intensively investigated with regards to its uptake mechanism and intracellular trafficking of  
448 nanoparticles and polyplexes, rendering it an optimal system for the evaluation of novel gene  
449 delivery systems and their transfection mechanism.<sup>54, 55</sup> Substantial influence of the utilized  
450 buffer system was observed. The cytotoxicity of **P1** is least influenced by the buffer  
451 ( $\text{IC}_{50, \text{PBS}} = 41.9 \text{ } \mu\text{g mL}^{-1}$ ,  $\text{IC}_{50, \text{HBG}} = 33.6 \text{ } \mu\text{g mL}^{-1}$ ) followed by **P2** ( $\text{IC}_{50, \text{PBS}} = 36.5 \text{ } \mu\text{g mL}^{-1}$ ;  
452  $\text{IC}_{50, \text{HBG}} = 18.8 \text{ } \mu\text{g mL}^{-1}$ ). In comparison, **P3** is substantially less toxic in PBS buffer, revealing  
453 the highest cell viability there ( $\text{IC}_{50, \text{PBS}} = 65.1 \text{ } \mu\text{g mL}^{-1}$ ,  $\text{IC}_{50, \text{HBG}} = 13.6 \text{ } \mu\text{g mL}^{-1}$ ) and showing

454 substantially lower toxicity than LPEI at similar concentrations. This could be attributed to a  
455 higher charge density of **P3** in acetate/HBG buffer in combination with an increased proportion  
456 of hydrophobic moieties leading to enhanced association with cellular membranes and thus to  
457 cytotoxic effects.<sup>56-58</sup> In contrast, it is assumed, that hydrophobic and cationic moieties are  
458 balanced in PBS buffer and excess cationic charges are shielded by the presence of phosphate  
459 ions leading to improved cytocompatibility.<sup>59</sup> To identify suitable conditions for evaluating the  
460 influence of the polymer structure on transfection efficiency L-929 cells were incubated with  
461 PBS or HBG polyplexes at various N/P ratios (2, 5, 10 and 20), pDNA concentrations (1.5, 3  
462 and 4.5  $\mu\text{g mL}^{-1}$ ) and incubation times (4 + 20 h, 24 h and 24 + 24 h) (data not shown).  
463 Considering these pretests, PBS and HBG polyplexes at N/P 5 and 10 and a pDNA  
464 concentration of 4.5  $\mu\text{g mL}^{-1}$  were selected for the further study and incubated with L-929 cells  
465 for 24 h, followed by further 24 h of incubation with fresh growth medium (24 + 24 h).  
466 Transfection efficiency was measured *via* flow cytometry as percentage of viable cells  
467 expressing EGFP (Figure 2B, S10, S15) and confirmed by fluorescence microscopy (Figure  
468 S16, S17). Cell viability was monitored by the sideward and forward scattering (FSC/SSC) of  
469 the cells (Figure S10).<sup>44</sup> In addition, cytotoxicity of polyplexes was evaluated *via* the  
470 PrestoBlue™ assay after 24 h of incubation (Figure S18). The cells showed high viability  
471 (> 85 % viable cells during transfection experiments (24 h + 24 h)). However, polyplexes  
472 prepared in HBG caused higher cytotoxicity in comparison to PBS polyplexes, whereas at the  
473 tested concentrations and N/P ratios no significant difference in transfection efficiency was  
474 observed. The highest percentage of transfected cells was reached with **P3** at N/P 10 in both  
475 buffers (20.7 % in PBS and 17.8 % in HBG), clearly outperforming **P1** and **P2** as well as the  
476 commercial control LPEI at the same conditions (12.7 % in PBS and 12.3 % in HBG). **P1**  
477 showed almost no transfection in PBS and HBG (N/P 10) (0.3 % and 1.0 % respectively),  
478 whereas **P2** resulted in 2.9 % in PBS and 3.7 % in HBG (N/P 10). Among the polypeptides, **P3**  
479 further resulted in the highest mean fluorescence intensity (MFI) (Figure S19) also visible by

480 fluorescence microscopy (Figure S16, S17). In contrast, hydrophobic cationic polypeptide  
 481 systems previously investigated by our group showed much lower transfection efficiency  
 482 compared to the commercial control LPEI.<sup>5</sup> Thus, the best performing **P3** polypeptide in this  
 483 study is a promising candidate for gene delivery not only because of its simpler synthesis and  
 484 higher synthetic variability, but also due to its substantially better performance in comparison  
 485 to LPEI.

486 To get a deeper understanding of the transfection mechanism of the polypeptides, the following  
 487 investigations were performed Since PBS polyplexes caused lower cytotoxicity in comparison  
 488 to HBG polyplexes, without any substantial difference in transfection efficiency, the  
 489 experiments were conducted exclusively with PBS polyplexes.

490



491

492 **Figure 2** Evaluation of cytotoxicity and transfection efficiency in L-929 cells. **A** Cytotoxicity  
 493 of **P1**, **P2** and **P3** without pDNA in the respective buffer was measured by the PrestoBlue™

494 assay following incubation of the cells (with the polymer) for 24 h. The dashed line indicates  
495 70 % cell viability and stars mark the polymer concentration required in the transfection studies  
496 for the respective N/P ratio at a pDNA concentration of  $4.5 \mu\text{g mL}^{-1}$  ( $n \geq 3$ ). **B** Transfection  
497 efficiency (EGFP expression) was investigated *via* flow cytometry after 24 h incubation with  
498 the polyplexes (N/P 5 and 10,  $4.5 \mu\text{g mL}^{-1}$  pDNA) followed by incubation with fresh growth  
499 medium for further 24 h (24 h + 24 h). Transfection efficiency is displayed as percentage of  
500 transfected cells in comparison to the control (polyplex with pKMyc pDNA) (mean  $\pm$  SD,  
501  $n \geq 3$ ). Statistically significant differences between the polypeptides in the respective buffer are  
502 denoted as follows:  $*p < 0.05$ ,  $**p < 0.01$ , and  $***p < 0.001$ .

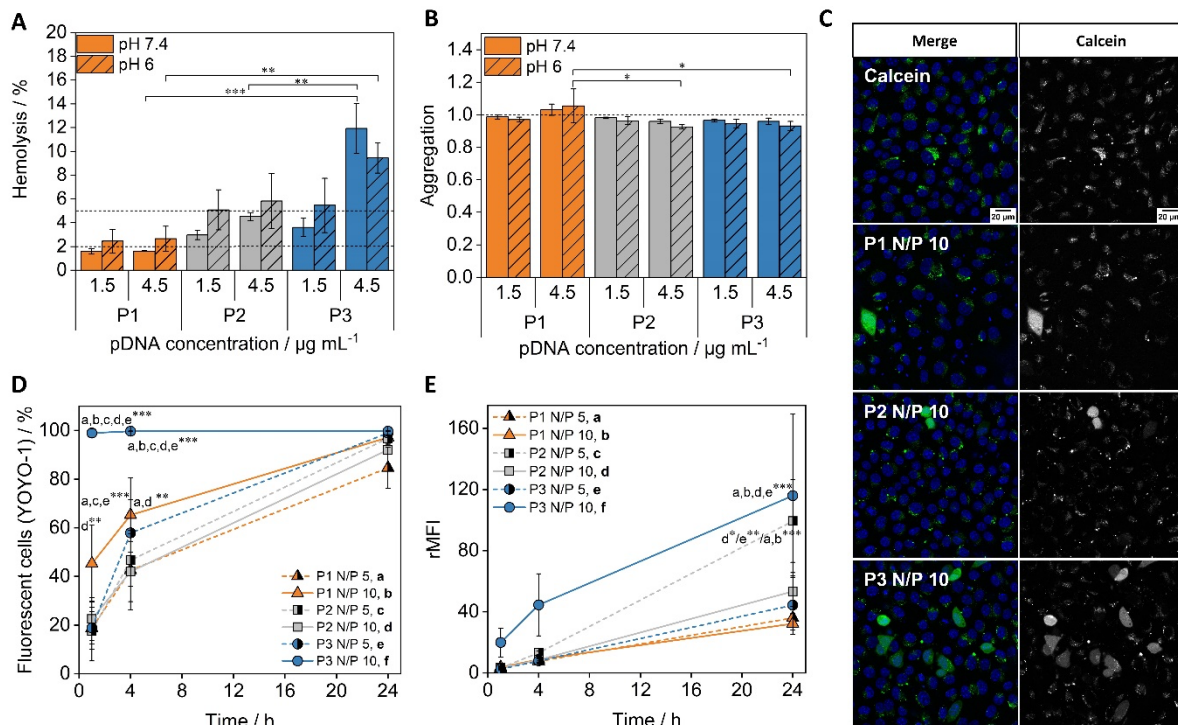
503

504 **Transfection mechanism in L-929 cells. Membrane Interactions and Endosomal Escape.**

505 Membrane interactions and endosomal escape are well-known obstacles for non-viral gene  
506 delivery and were studied by a hemolysis/aggregation and a calcein release assay. Erythrocytes  
507 were incubated with PBS polyplexes at N/P 10 at various pDNA concentrations and pH values  
508 to study membrane interactions at physiological (pH 7.4) and endosomal (pH 6) conditions.<sup>60</sup>  
509 Then, hemoglobin release was measured as indicator for membrane disruption (Figure 3A).  
510 Additionally, erythrocyte aggregation was monitored, likewise an indicator for polymer-  
511 membrane interactions (Figure 3B). An ascending hemolytic trend was observed at both pH  
512 values, with **P3** showing the strongest hemolytic activity especially at high concentrations  
513 ( $11.9 \pm 2.1$  %). An opposing trend emerged for aggregation, with **P1** resulting in slight  
514 aggregation at high concentrations (1.03 at pH 7.4 and 1.06 at pH 6), whereas **P2** and **P3** did  
515 not show any effect (aggregation  $< 1.0$ ). This proposes a different mechanism of membrane  
516 interaction for **P1**, showing merely membrane association, whereas **P2** and **P3** clearly lead to  
517 membrane leakage events. This can be attributed to the increasing proportion of HexA groups  
518 in **P2** and **P3** promoting additional hydrophobic membrane interactions, whereas the cationic  
519 homopolymer **P1** mainly interacts electrostatically.<sup>57, 61</sup> The formation of ordered secondary  
520 structures might also contribute to the hemolytic activity of **P3** at both physiological and  
521 endosomal pH values.<sup>19, 59</sup> These results point towards a high cellular uptake as well as efficient  
522 endosomal escape of **P3**, which could explain its good transfection performance.



523 To study endosomal release, a calcein release assay was performed. The cells were incubated  
 524 simultaneously with the membrane impermeable dye calcein and the polyplexes at N/P 10 for  
 525 1 h and subsequently imaged *via* CLSM (Figure 3C, Figure S20). Endosomal release indicated  
 526 by homogeneous fluorescence of calcein within the cytosol was observed for all polypeptides,  
 527 with **P3** showing the highest percentage of calcein releasing cells ( $8.2 \pm 3.1$  %, Figure S21),  
 528 which is in accordance with the hemolytic activity at pH 6 (Figure 3A). However, differences  
 529 within the polypeptides were rather small ( $4.9 \pm 2$  % for **P1** and  $5.7 \pm 3.8$  % for **P2**). This  
 530 indicates that the endosomal release efficiency may not be the main factor contributing to the  
 531 superior transfection efficiency of **P3**.



532  
 533 **Figure 3** Investigation of the gene delivery process in L-929 cells. **A** Hemolytic activity was  
 534 measured as release of hemoglobin from sheep erythrocytes after incubation with the  
 535 polyplexes (N/P 10, 1.5 and 4.5 mg mL<sup>-1</sup> pDNA). Erythrocytes were incubated with the  
 536 polyplexes at pH 7.4 and 6 to mimic conditions present in the blood and the endosomes,  
 537 respectively (mean ± SD, n = 3). **B** Aggregation of erythrocytes incubated with the polyplexes  
 538 was measured as light absorption of erythrocytes. 10 kDa branched poly(ethylenimine) was  
 539 used as positive control and PBS as negative control (mean ± SD, n=3). Statistically significant  
 540 differences at the respective concentration and pH value are denoted as follows: \**p* < 0.05,  
 541 \*\**p* < 0.01, and \*\*\**p* < 0.001. **C** Representative images of the endosomal escape of polyplexes  
 542 analyzed *via* CLSM are shown. Cells were incubated simultaneously with the polyplexes  
 543 (N/P 10, 4.5 µg mL<sup>-1</sup> pDNA) and the non-permeable dye calcein (green) for 1 h. After  
 544 incubation, the cells were washed twice, and nuclei were further stained with Hoechst (blue).  
 545 **D + E** Time-dependent uptake of polyplexes formulated in PBS was measured *via* flow

546 cytometry. L-929 cells were incubated with polyplexes (N/P 5 and 10, 1.5  $\mu\text{g mL}^{-1}$  pDNA) for  
547 1, 4 or 24 h. Cellular uptake is plotted as **D** percent of cells showing increased fluorescence  
548 compared to the control (YOYO-1 stained pDNA) and **E** relative mean fluorescence intensity  
549 (rMFI) of viable single cells, calculated relative to the control (YOYO-1 stained pDNA)  
550 (mean  $\pm$  SD, n = 3). Statistically significant differences at the respective timepoints are  
551 indicated as follows: \* $p < 0.05$ , \*\* $p < 0.01$ , and \*\*\* $p < 0.001$ .

552  
553

554 *Cellular Uptake via Flow Cytometry.* To study cellular uptake in a time-dependent manner,  
555 L-929 cells were incubated with YOYO-1 labeled polyplexes up to 24 h. The percentage of  
556 cells with increased YOYO-1 fluorescence (YOYO-1 positive cells) and the rMFI were  
557 measured quantitatively *via* flow cytometry (Figure 3D, E, S22). Cellular uptake of all polymers  
558 is time-dependent and reached > 90 % YOYO-1 positive cells after 24 h, whereas **P3** (N/P 10)  
559 polyplexes required only 1 h for this (99.8 % YOYO-1 positive cells). The highest rMFI values  
560 were found for **P2** N/P 5 and **P3** N/P 10 polyplexes after 24 h (99.4 and 116.0 respectively),  
561 hence these were later examined in greater detail. The lowest rMFI was observed for **P1** even  
562 after 24 h (35.9 at N/P5 and 32.2 at N/P 10), which is in accordance with its low transfection  
563 efficiency. Investigation of uptake patterns measured *via* flow cytometry further underline the  
564 differences within the used polypeptides (Figure S22). While the population of YOYO-1  
565 positive cells homogeneously shifts to higher FI values for **P3** N/P 10 polyplexes over time,  
566 only partial and broader shifts are observed for **P1** and **P2**. This indicates a homogeneous uptake  
567 of **P3** N/P 10 polyplexes, complementing the transfection results with a high number of  
568 transfected cells with high rMFI.

569 As the polyplex size is a crucial parameter influencing cellular uptake, dynamic light scattering  
570 (DLS) measurements were conducted (Figure S23, Table S4). **P3** N/P 10 polyplexes had a  
571 diameter (z-average) of 140 nm and a PDI of 0.16, while all other polypeptides and **P3** N/P 5  
572 showed diameters > 1000 nm, a PDI of > 0.38 and inappropriate correlation coefficients (Figure  
573 S23), indicating the formation of larger aggregates within the samples, which might be  
574 overestimated in DLS measurements and, thus, rendering this characterization method

575 unsuitable for these samples. Therefore, more detailed size measurements of selected samples  
576 were performed, employing nanoparticle tracking analysis (NTA) and imaging methods  
577 including cryogenic transmission electron microscopy (cryo-TEM), fluorescence microscopy  
578 (*chapter 3.5.3.*), and TEM measurements after incubation with cells (*chapter 3.5.4.*), all  
579 identifying nano-sized particles as well. Nanoparticle tracking analysis (NTA) measurements  
580 were conducted for **P3** N/P 10 and **P2** N/P 5, both showing the highest uptake in L-929 cells  
581 (Figure S24, Table S5), with measurements of **P3** N/P 10 complementing the DLS results with  
582 a mean diameter of 196 nm. Aggregate formation for **P2** N/P 5 was confirmed, however after  
583 separation of the aggregates by centrifugation, nanostructures with a mean diameter of 258 nm  
584 were measured, which were not detectable by DLS in the presence of aggregates. For potential  
585 *in vivo* applications, such aggregates can be separated by additional processing steps, *e.g.* by  
586 centrifugation or filtration. These differences in polyplex sizes and aggregation behavior may  
587 explain the differences in uptake levels in particular at shorter incubation times as particle sizes  
588 below 200 nm are promoting controlled cellular uptake by endocytosis, while aggregation  
589 results in lower or at least slower and less controlled uptake by cells.<sup>62</sup> This might influence  
590 transfection efficiencies, with **P3** N/P 10 polyplexes being taken up in a controlled and  
591 homogeneous manner, whereas only the nanosized portion of **P2** N/P 5 structures shows  
592 controlled uptake, and the portion of large aggregates present in the sample is either not taken  
593 up within short time periods or only occasionally by few cells.<sup>63</sup> Cryo-TEM measurements of  
594 **P3** N/P 10 polyplexes showed nanostructures in the size range of approx.  $\leq 100$  nm in diameter  
595 with slight aggregation (Figure S25). This size range is slightly smaller than intensity-weighted  
596 diameters within DLS measurements but is complementing the number-weighted diameters.  
597 The polyplexes appeared as particles with an uneven boundary, thus representing a structure  
598 and morphology in between classical polymer nanoparticle and hydrophilic polyplexes.<sup>64, 65</sup>  
599 The observation of such structures is in line with a previous study of us exploring amphiphilic  
600 methacrylates for gene delivery.<sup>66</sup> Besides particle size and morphology, the surface charge

601 plays a crucial role in cellular uptake and transfection efficiency.<sup>67, 68</sup> Therefore, zeta potential  
602 measurement of polyplexes were conducted (Table S4). The polyplexes had a similar positive  
603 zeta potential independent of the N/P ratio and polymer (+ 21.2 to 22.8 mV). It is thus assumed  
604 that the surface charge is no decisive factor for the cellular uptake of the polyplexes within this  
605 study.

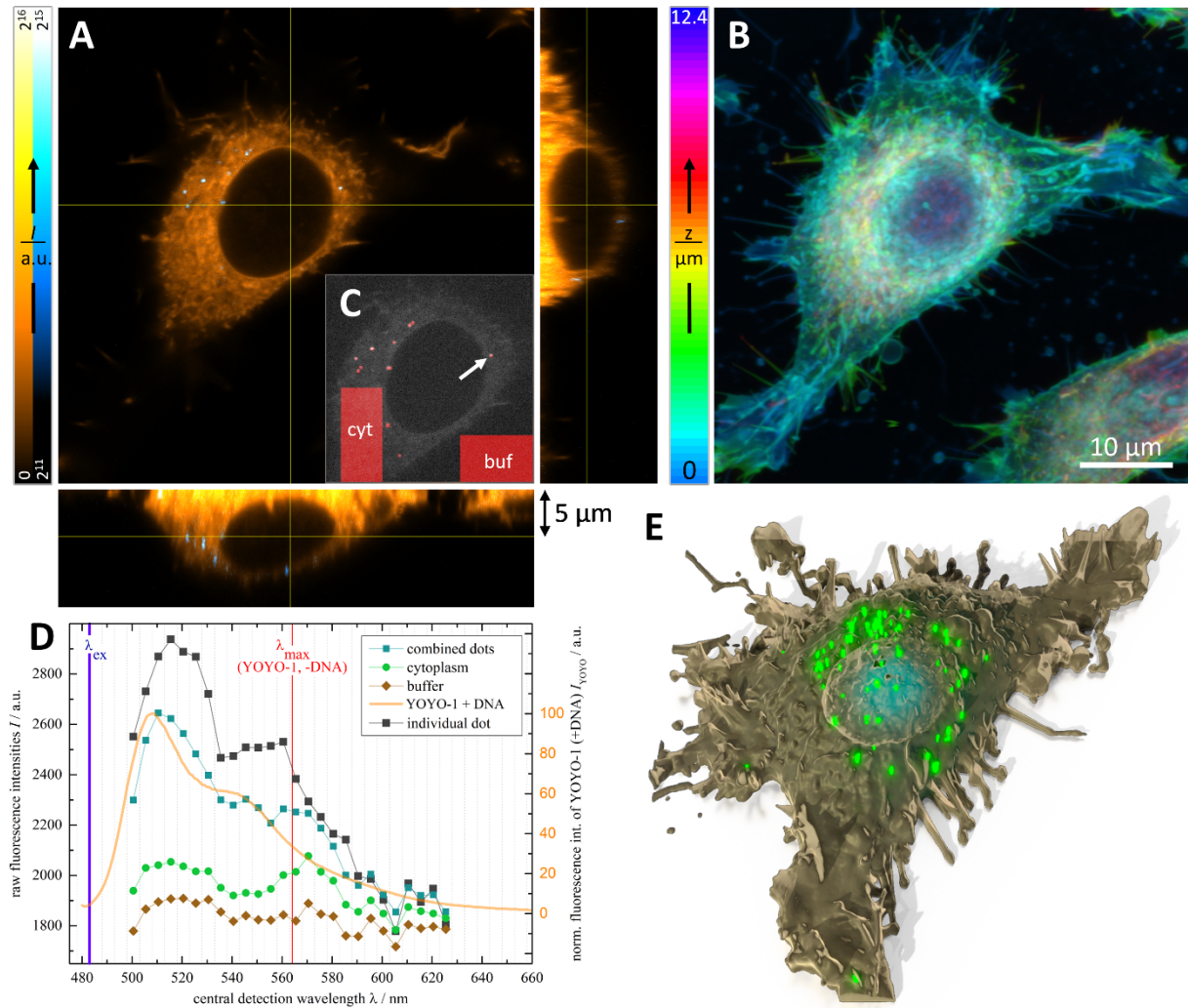
606

607 *Details of Cellular Uptake Visualized by Fluorescence Microscopy.* To analyze the uptake  
608 mechanism in more detail, the most promising polyplexes, **P2** N/P 5 and **P3** N/P 10, were  
609 further investigated in L-929 cells using fluorescence microscopy. For this purpose, polyplexes  
610 labeled with intercalated YOYO-1, in conjunction with cell membrane staining by CMDR,  
611 were used. The dyes are spectrally fully separated with regard to both their excitation and  
612 emission, enabling simultaneous imaging. No qualitative differences regarding polyplex uptake  
613 and distribution could be detected after incubation with **P3** or **P2** polyplexes in a series of z-  
614 resolved (Video S1, Figure 4, S26-30) and time-resolved measurements of L-929 cells (Videos  
615 S2-S4, Figure S31-40). Thereby, Video S4 shows a **P3** polyplex settling to the substrate surface,  
616 being subsequently 'found' by a lamellipodium and transported to the cell, before being  
617 encapsulated and endocytically taken up (marked by a white arrow), representing an interesting  
618 observation of the initial interaction of the polyplexes with the cells. A detailed discussion of  
619 this interaction and approaching of the polyplexes to the cell surface together with their uptake  
620 dynamics is provided below. Interestingly, fixated **P3**-incubated cells, which were stored in the  
621 fridge overnight after fixation showed signs of polyplex disintegration as evidenced by diffuse  
622 fluorescence from several locations, predominantly in areas of former hotspots of polyplex  
623 uptake (Figure S28). Contrastingly, polyplexes in the main cell body seemed to be unaffected  
624 (Figure S27). As already mentioned, we did not observe qualitative differences in the uptake  
625 behavior and also the initial interaction of the cells with the polyplexes in time- and z-resolved  
626 measurements between **P2** and **P3** polyplexes, but a slight focus drift in the time-resolved **P3**

627 measurements limited their analysis and, hence, a more detailed discussion of the **P2**  
628 measurements is given in the following.

629 High resolution overview images of fixated, **P2**-incubated cells in the bottom-most layer, *i.e.*,  
630 the glass-cell interface, and 2.4  $\mu\text{m}$  above were recorded (Figure S41-S43). These illustrate the  
631 cell structures and organization, particularly the dense network of filopodia emerging from each  
632 cell and interconnecting it with its neighboring cells (Figure S41). In the YOYO-1 channel  
633 (Figure S42, 43), bright dots with an apparent size (full width at half maximum of point spread  
634 function  $(\text{FWHM})_{\text{PSF},xy}(488 \text{ nm}, 1\text{AU}, 1.4 \text{ NA}) \approx 178 \text{ nm}$ ) of approximately 250 nm to 400 nm  
635 located in the cytoplasm of some, but not all, cells indicate that uptake took place (0–12 dots  
636 per cell, avg.: 2.4,  $n = 26$ ). These observations complement the NTA measurements of  
637 centrifuged **P2** polyplexes confirming the presence of nanoparticles of approx. 300 nm in  
638 diameter besides larger aggregates (Figure S24 Table S5). However, due to the small particle  
639 size in combination with a relatively high z-resolution, these data do not allow for reliable  
640 quantitative statements about the number of dots (meaning polyplexes) per cell, because that  
641 would depend strongly on the imaged plane. For individual cells and small groups of cells this  
642 can be circumvented by z-resolved measurements. Figure 4A and Video S1 provide an example  
643 of this approach. While in any given plane in this cell, the maximum number of bright dots we  
644 were able to observe was 12, a 3D reconstruction (Figure 4E) revealed a total of 77 bright dots  
645 that are scattered mostly around the nucleus. Additionally, a multitude of filopodia and intricate  
646 intracellular features are visible, contextualizing the positional information (Figure 4B). The  
647 time requirements for this procedure, however, are prohibitive for studying larger numbers of  
648 cells, and this microscopic approach, therefore, requires statistically more powerful techniques  
649 like the above discussed flow cytometry to complement it. To confirm the observed particles'  
650 identification as YOYO-1 containing polyplexes, spectrally resolved measurements (Figure 4C,  
651 4D) were taken in the plane indicated in Figure 4A. The combined emission spectra of all  
652 11 dots closely resembles the fluorescence spectrum of DNA-intercalated YOYO-1,<sup>69</sup>

653 confirming the identification of these dots as polyplexes. Slight deviations at about 570 nm may  
 654 be due to free YOYO-1. Noteworthy, for some of the more intense and thus less noisy dots, it  
 655 is possible to obtain meaningful spectra of individual polyplexes, as exemplified in Figure 4D.



656

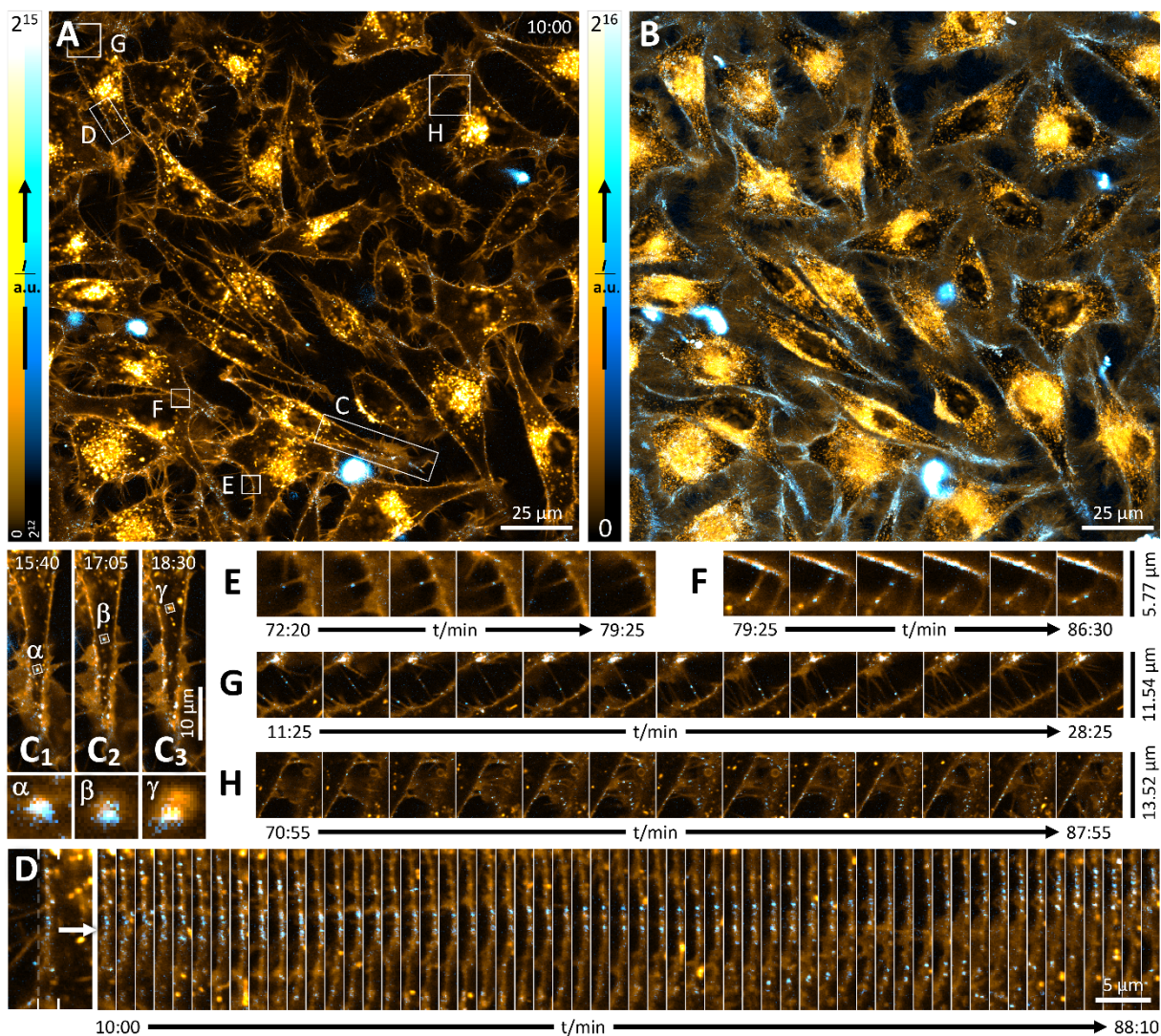
657 **Figure 4** z-Resolved and  $\lambda$ -resolved fluorescence microscopy images of L-929 cells after  
 658 incubation with **P2** N/P 5 polyplexes (15 min) and PFA fixation. **A** z-Stack with orthogonal  
 659 views at positions indicated by yellow lines. The central image depicts the plane 5  $\mu\text{m}$   
 660 above the microscope slide in which the subsequent  $\lambda$ -scan was performed. Orange: CDMR  
 661 fluorescence, blue-cyan: YOYO-1 fluorescence indicating polyplexes. Intensities are scaled  
 662 linearly along the indicated color bars. **B** Maximum intensity projection (MIP) of the CDMR  
 663 channel of the same z-stack after intensity adjustment ( $I_{\text{new}} = (1 + 0.075z)I_{\text{old}}$  with  $z = 0 \dots 62$   
 664 being the slice number) and color coding along the z-axis. **C** MIP along the  $\lambda$ -axis of an  
 665 emission scan ( $\lambda_{\text{ex}} = 483 \text{ nm}$ ,  $\Delta\lambda_{\text{det}} = 5 \text{ nm}$ ). Eleven polyplexes were manually identified (red  
 666 overlay). **D** Emission spectra of cytoplasm, PBS, and polyplexes, averaged over all respectively  
 667 labeled pixels in **C**, alongside an individual polyplex (marked by white arrow in) spectrum and  
 668 a reference spectrum of YOYO-1+DNA, normalized to the average polyplex spectrum  
 669 (YOYO-1+DNA spectrum obtained from Thermo Fisher Scientific). Purple line: excitation  
 670 wavelength, dotted grid lines: detection window boundaries, red line: emission maximum of  
 671 free YOYO-1. **E** 3D reconstruction of the respective cell with polyplexes marked as green dots,

672 depicting their distribution around the nucleus. A total of 77 polyplexes was identified, notably,  
673 none of which stuck to the outer cell membrane.  
674

675 To monitor the uptake behavior of polyplexes and the approaching of the polyplexes to the cell  
676 surface, a time series of living cells was recorded after addition of the polyplex solution (10 min  
677 to 88 min after addition, Video S2). During the first 10 min after addition, the polyplexes could  
678 be observed settling onto the glass substrate and cells (not shown), whereas no dots were visible  
679 in the YOYO-1 channel before polyplex addition (Figure S31). Figure 5A shows the first frame  
680 of the time series. Large numbers of polyplexes are stuck to the cell membranes but only some  
681 cells have small numbers of polyplexes in the cytoplasm in the imaged plane. After 88 min, all  
682 cells in the field of view show polyplexes in the cytoplasm, though the amounts vary from  
683 below 10 to several dozens. In all cases, internalized polyplexes coincide with bright spots in  
684 the CMDR channel, indicating encapsulation in membrane vesicles and endocytosis as uptake  
685 mechanism. Illustrations emphasizing these effects are given in the SI, Figure S32-37. A  
686 discrete uptake event is documented in Figure S38. The uptake appears to happen  
687 predominantly, if not exclusively, at the tip of cell extrusions in the immediate vicinity of  
688 lamellipodia. These are also the areas of highest polyplex density and strongest polyplex  
689 agitation (Video S2), with the latter being a result of rapid filopodium and lamellipodium  
690 movement. In combination with the relative flatness of those areas (as compared to the main  
691 cell bodies), confining the polyplex movement mostly to two dimensions (*i.e.*, the imaging  
692 plane), this leads to prominent hotspots in the lamellipodial/filopodial region in a maximum  
693 intensity projection (MIP) along the time axis of the series (Figure 5B). The highly dynamic  
694 movement of filopodia leads to a hazy glow around the mostly stationary cells in this  
695 representation, showing that very few areas remain ‘unexplored’ by the cell cluster. Once taken  
696 up, we observed the polyplex containing vesicles being rapidly transported towards the cell  
697 center in most cases, as illustrated in Figure 5C. In linear approximation, the distance covered  
698 from C1 to C2 and from C2 to C3 was 5.8  $\mu\text{m}$  each, corresponding to a transport velocity of

699  $4.09 \mu\text{m min}^{-1}$ . We did not observe discrete uptake events in regions other than the above  
700 described, though it should be noted that high polyplex mobility on the cell membrane could  
701 be seen, leading to them frequently drifting into and out of focus and making it difficult to  
702 follow individual polyplexes for prolonged amounts of time. Figure 5D illustrates this drifting  
703 motion within the imaging plane. It appears to be largely passive without strong directional  
704 preferences. It can be assumed that this motion is not confined to two dimensions as individual  
705 polyplex traces in Figure 5D get darker and lighter in an unpredictable manner with some  
706 vanishing completely or suddenly appearing. This membrane drifting probably plays a role in  
707 supplying the endocytically active lamellipodia regions with polyplexes <sup>13</sup>.

708



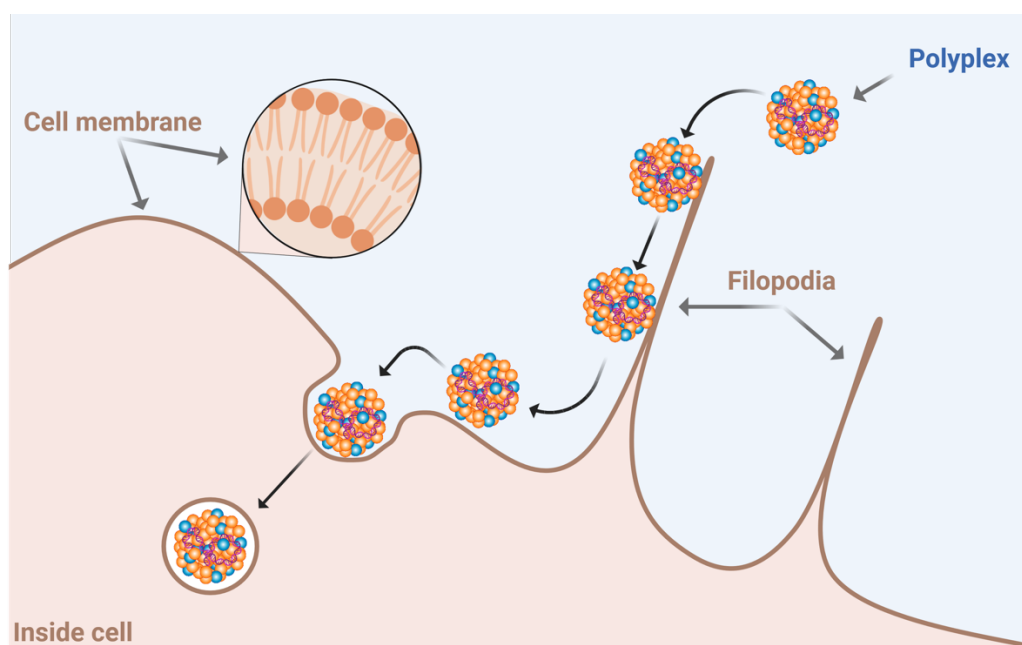
709 **Figure 5** Time series of fluorescence images (orange: CMDR, cyan-blue: YOYO-1) of L-929  
710 cells after addition of polypeptide polyplex (P2). A First image ( $t = 10$  min) of the series. Cell  
711



712 membranes are clearly distinguishable by CMDR staining. Each cell has a multitude of  
713 filopodia. Polyplexes have settled on the cells and stick to the membranes. **B** MIP of the series  
714 along the time axis from 10 to 88 min. **C** Series of three consecutive frames showing the rapid  
715 transport of a polyplex-containing vesicle from the lamellipodium towards the main cell body  
716 after endocytosis. Inserts  $\alpha$ - $\gamma$  have side lengths of 1.8  $\mu\text{m}$ . **D** Polyplexes passively sliding along  
717 the cell membrane without strong directional preferences and with no cellular uptake occurring.  
718 All 56 frames are depicted. **E** Filopodium surfing of a single polyplex towards the membrane  
719 of the cell body. **F** A single polyplex is transferred from the membrane of one cell to that of  
720 another *via* filopodium surfing. **G** Filopodium bridges between cells mediate polyplex  
721 exchange. **H** Lamellipodium of one cell touches another cell's membrane. Large numbers of  
722 polyplexes are transported *via* the gap in a relatively short time span.

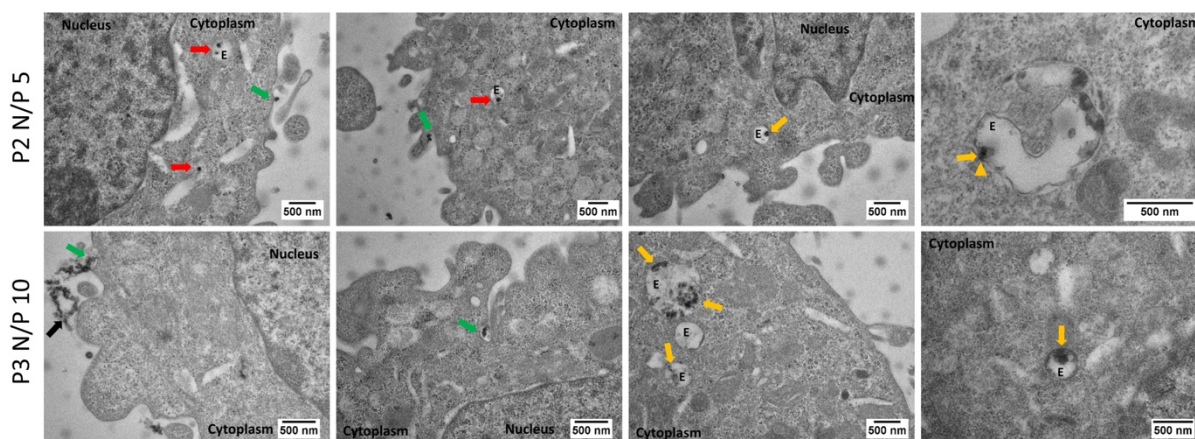
723  
724 As mentioned above, an interesting observation is the mode of polyplex acquisition and initial  
725 interaction with the cells. In contrast to those polyplexes, which initially settle on the cells,  
726 others are actively transported from the vicinity towards the cells *via* filopodium surfing by a  
727 large number of filopodia, constantly exploring the cells' surroundings.<sup>13, 70</sup> One of the  
728 numerous examples of this effect is depicted in Figure 5E. This surfing motion appears to be  
729 independent of filopodium retraction,<sup>71</sup> though in many cases these effects are difficult to  
730 separate. Particularly interesting in this regard is the role of cell-bridging filopodia. In areas of  
731 close contact, stretches of the cell membrane with more than 1 bridging filopodium per 1  $\mu\text{m}$   
732 are not uncommon, often with unclear filopodium affiliation (compare also Figure S41). These  
733 bridges can be brief contacts, lasting only for a few minutes, but also remarkably long-lived  
734 with examples in the here discussed dataset lasting for almost 1 h. Polyplex transport along  
735 those bridges occurs as for non-bridging filopodia (Figure 5G). While in many cases the  
736 polyplex origin is unclear, in others, filopodia of one cell clearly detach polyplexes from  
737 another cell's membrane and subsequently acquire it (Figure 5F). A similar transfer effect can  
738 be observed where lamellipodia of one cell touch another cell's membrane (Figure 5H), though,  
739 again, the polyplex' origin remains unclear in this example. These findings (regarding the role  
740 of lamellipodia and filopodia in the initial contact of cells with particle like structures such as  
741 polyplexes, their acquisition and transport by surfing on and retraction of filopodia and cell-  
742 to-cell distribution) have been firstly shown for viruses attaching to the filopodia and surfing  
743 towards the cell surface and main body where they are taken up by the cell.<sup>72, 73</sup> Subsequent to

744 reaching the cell surface by help of the filopodia, the particle like structures are taken up by  
745 several endocytic processes, *e.g.*, clathrin- and caveolae-mediated endocytosis and  
746 macropinocytosis, ending up in the endolysosomal pathway (early endosomes), which is  
747 usually desired for non-viral gene delivery systems.<sup>74, 75</sup> The uptake thereby often occurs in the  
748 endocytically active lamellipodia regions as also observed within this study.<sup>13</sup> This mechanism  
749 of acquisition followed by endocytic uptake can be probably attributed to the enrichment of  
750 proteoglycan receptors such as syndecans on filopodia, known to facilitate interaction with  
751 cationic particles such as cationic non-viral vectors.<sup>72, 76</sup> However, so far little is known about  
752 the initial interaction and approaching of non-viral gene delivery vectors to cells and the role  
753 of this mechanism in the transfection process is largely unrecognized and underappreciated, as  
754 only few studies investigated this mechanism for lipoplexes and hydrophilic polyplexes.<sup>13, 70</sup> In  
755 this study, it has now firstly been shown that this mechanism also plays a role for amphiphilic  
756 polyplexes and their subsequent cellular internalization and is thus an important aspect and  
757 promising approach for further optimizing the transfection efficiency of such polyplexes in  
758 future studies. The proposed mechanism is shown in simplified form in Scheme 1.



759  
760 **Scheme 1** Proposed mechanism of polyplex acquisition and their transport by surfing on  
761 filopodia.

762 *Cellular Uptake Measured via Transmission Electron Microscopy.* In order to further evaluate  
763 the uptake mechanism following polyplex acquisition by the lamellipodia and filopodia and the  
764 intracellular polyplex location, TEM measurements of L-929 cells incubated with **P2** N/P 5 and  
765 **P3** N/P 10 polyplexes for 1 h were conducted. It was possible to identify several cellular  
766 substructures, *e.g.*, the nucleus and endolysosomal vesicles within the obtained TEM images.  
767 Further structures with high electron density were observed, which were attributed to **P2** and  
768 **P3** polyplexes that were stained with uranyl acetate.<sup>77</sup> In both samples, the polyplexes appear  
769 as nearly spherical nanosized structures and for **P3** N/P 10, partial agglomeration of polyplexes  
770 in the extracellular environment was observed, which is in line with the cryo-TEM  
771 measurements (Figure S 25). Both samples show location of single or multiple nanosized  
772 polyplexes in endolysosomal vesicles. These observations complement the NTA measurements  
773 of centrifuged **P2** polyplexes and the fluorescence microscopy measurements, again confirming  
774 the presence of nanosized polyplexes besides larger aggregates (Figure S24, Figure 5, Table  
775 S5). Furthermore, these results illustrate that larger aggregates are not taken up by cells within  
776 an hour, which correlates with the fluorescence microscopy measurements. Subsequent to  
777 cellular uptake, within the endolysosomal vesicles, polyplexes are often associated with the  
778 vesicle membranes and partially result in membrane deformation. These results confirm the  
779 active endocytic uptake of **P2** and **P3** polyplexes into L-929 cells as observed by fluorescence  
780 microscopy.<sup>78, 79</sup> However, no qualitative differences between **P2** and **P3** regarding location or  
781 membrane interaction were observed in TEM measurements following 1 h incubation.



782  
 783 **Figure 6** TEM images of L-929 cells incubated with **P2** N/P 5 and **P3** N/P 10 polyplexes for  
 784 1 h. Electron dense structures (black) were identified as polyplexes. Black arrows indicate  
 785 extracellular accumulation of polyplex structures. Green arrows indicate polyplex-cell  
 786 interaction or uptake events. The location of polyplexes in vesicles, *e.g.*, endosomes (E) is  
 787 indicated by red arrows. Yellow arrows indicate interaction of polyplexes with vesicle  
 788 membranes and the deformation of these membranes by polyplexes is indicated by yellow  
 789 arrow heads.

790 In summary, a filopodia- and lamellipodia-based endocytic uptake mechanism was observed  
 791 for both **P3** N/P 10 polyplexes and the nanosized portion of **P2** N/P 5 polyplexes. Quantitative  
 792 flow cytometry measurements revealed faster and more homogeneous uptake kinetics for **P3**  
 793 N/P 10 compared to **P2** N/P 5 polyplexes, but the uptake levels (percentage of cells, rMFI) after  
 794 24 h were similar (Figure 3E). Notwithstanding, the transfection efficiency is substantially  
 795 higher for **P3** N/P 10 after 24 h incubation. This might be explained by higher endosomal  
 796 release efficiency observed after 1 h, facilitated by higher membrane interaction of the **P3**  
 797 polymer and faster polyplex uptake resulting in high endosomal polyplex concentration.<sup>80</sup>  
 798 Nevertheless, the escape efficiency is rather low and not substantially higher than for **P1** and  
 799 **P2**. This leads to the assumption that endosomal escape might take place over longer time  
 800 periods, steadily releasing the polyplexes resulting in higher transfection efficiency compared  
 801 to the other polypeptides.

## 802 CONCLUSION

803 A selected number of amphiphilic polypeptides containing different distributions of cationic  
 804 AB-L-Gln (100, 84, 60, 30 and 0 mol%) and aliphatic Hex-L-Gln (0, 16, 40, 70 and 100 mol%)  
 805 side chains were obtained *via* an efficient four-step synthesis. It was shown that the secondary

806 structure of P(AB-L-Gln-*stat*-Hex-L-Gln) can be influenced by varying the distribution of both  
807 cationic and aliphatic units.

808 The water-soluble polypeptides **P1**, **P2** and **P3** were evaluated for their ability to complex  
809 pDNA, showing sufficient binding and release capability. An intensive screening of the  
810 transfection performance of the polyplexes in the mouse fibroblast cell line L-929 revealed **P3**  
811 as clear outperformer over the other polypeptides and commercial LPEI. Polyplexes formed  
812 with the **P3** polypeptide comprising the highest proportion of hydrophobic HexA groups and  
813 highest amount of ordered secondary structures such as  $\alpha$ - helical and  $\beta$ -sheet structures  
814 resulted in the highest percentage of EGFP expressing cells in comparison to **P1** and **P2** at  
815 similar N/P ratios and, thus, similar amount of cationic charges, while maintaining high cell  
816 viability. In-depth investigation of the interaction with erythrocyte membranes as a model  
817 system and with L-929 cells illustrated the highest membrane interaction and endosomal release  
818 levels of **P3** polyplexes. Evaluation of cellular uptake by flow cytometry revealed that **P3**  
819 polyplexes were taken up by almost all cells after 1 h, which was observed for **P2** polyplexes  
820 only after a longer incubation period. This difference was attributed to the presence of larger  
821 aggregates besides nanosized polyplexes in **P2**. Time- and z-resolved fluorescence microscopy  
822 and TEM demonstrated an active filopodia- and lamellipodia-based initial acquisition of the  
823 nanosized polyplexes present in **P2** and **P3** followed by endocytic uptake mechanisms for both  
824 polypeptides, showing no qualitative difference within the polypeptides. In both cases, cells  
825 were found to actively explore the surroundings with their filopodia and acquire the polyplexes  
826 before transporting them towards the main cell body, predominantly by filopodium surfing,  
827 possibly in combination with filopodium retraction. The polyplexes presented here exhibited  
828 high mobility on the cell surface, where they can reside for prolonged amounts of time. Polyplex  
829 uptake appears to happen in a strictly localized fashion in the very active lamellipodia regions,  
830 followed by active transport to the cell interior. In combination with higher endosomal release

831 efficiency, facilitated by higher membrane interaction, the faster and more homogenous  
832 polyplex uptake mediated by filopodia- and lamellipodia-based initial acquisition resulted in  
833 substantially higher transfection efficiency of the **P3** polypeptide outperforming the other  
834 polypeptides.

835 Taken together, these results give insight into the gene transfer process of amphiphilic  
836 polypeptides including the mechanism of initial polyplex acquisition and internalization and  
837 reveal the potential of the integration of aliphatic groups into cationic polypeptides to obtain  
838 nanosized, effective, biocompatible, and potentially biodegradable gene delivery vectors. The  
839 straightforward and versatile synthesis of polypeptides by post-polymerization  
840 functionalization provides a promising platform for further optimization and fine-tuning in  
841 terms of charge, hydrophobicity, secondary structure, and the introduction of shielding units  
842 such as PEG in order to develop highly efficient amphipathic polypeptides that are capable of  
843 overcoming the physiological barriers faced when delivering pDNA but also other cargos such  
844 as siRNA and mRNA *in vitro* and *in vivo*. Imaging techniques such as fluorescence microscopy  
845 and transmission electron microscopy help understanding the involved processes and  
846 interactions on a subcellular level and in particular allow to study the so far largely  
847 unrecognized and for amphiphilic polypeptides unstudied lamellipodia- and filopodia-based  
848 mechanism of initial interaction of the with cells. This offers the possibility for further design  
849 and optimization of tailor-made polypeptide-based vectors.

## 850 **ASSOCIATED CONTENT**

### 851 **Supporting information**

852 The datasets used and/or analyzed during the current study are available from the corresponding  
853 author on reasonable request. Additional material, methods, and results, including Figure  
854 S1 - S43, Tables S1 - S5, Videos S1 - S4, are collected in the Supplementary Information.

855

856 **FUNDING**

857 This work was financially supported by the Collaborative Research Center PolyTarget (SFB  
858 1278 - projects B01, C01, Z01, project ID 316213987) funded by the German Research  
859 Foundation (DFG). TEM and cryo-TEM investigations were performed at the electron  
860 microscopy facilities of the Jena Center for Soft Matter (JCSM), which were purchased with  
861 grants from the DFG and the European funds for Regional Development (EFRE). Furthermore,  
862 the authors thank the Bundesministerium für Bildung und Forschung (BMBF, Germany,  
863 #13XP5034A PolyBioMik). The LSM8800 ELYRA PS.1 was kindly funded by the DFG.

864 **NOTES**

865 The authors declare that they have no competing interests. Scheme 1 was created using  
866 BioRender.

867 **ACKNOWLEDGEMENTS**

868 The authors thankfully acknowledge Carolin Kellner, Bärbel Beringer-Siemers,  
869 Elisabeth Preußger and Maria Stumpf for their excellent technical support and Dr. Grit  
870 Festag for maintaining the SEC facilities. Furthermore, the authors thankfully  
871 acknowledge Elisabeth Moek for support with the transfection assays and Constanze  
872 Schulz and Arnica Karuna for support with fluorescence microscopy measurements.  
873 The authors gratefully thank Prof. U. S. Schubert for providing excellent facilities and  
874 his continuous support.

## REFERENCES

- (1) Salas-Ambrosio, P.; Tronnet, A.; Verhaeghe, P.; Bonduelle, C. Synthetic Polypeptide Polymers as Simplified Analogues of Antimicrobial Peptides. *Biomacromolecules* **2021**, *22*, 57-75.
- (2) Sang, X.; Yang, Q.; Wen, Q.; Zhang, L.; Ni, C. Preparation and Controlled Drug Release Ability of the Poly[N-Isopropylacrylamide-co-Allyl Poly(Ethylene Glycol)]-b-Poly( $\gamma$ -Benzyl-L-Glutamate) Polymeric Micelles. *Mater. Sci. Eng. C* **2019**, *98*, 910-917.
- (3) Tesauro, D.; Accardo, A.; Diaferia, C.; Milano, V.; Guillon, J.; Ronga, L.; Rossi, F. Peptide-Based Drug-Delivery Systems in Biotechnological Applications: Recent Advances and Perspectives. *Molecules* **2019**, *24*, 351-377.
- (4) Zeng, X.; Wang, L.; Liu, D.; Liu, D. Poly(L-Lysine)-Based Cylindrical Copolypeptide Brushes as Potential Drug and Gene Carriers. *Colloid Polym. Sci.* **2016**, *294*, 1909-1920.
- (5) Klemm, P.; Behnke, M.; Solomun, J. I.; Bonduelle, C.; Lecommandoux, S.; Traeger, A.; Schubert, S. Self-Assembled PEGylated Amphiphilic Polypeptides for Gene Transfection. *J. Mater. Chem. B* **2021**, *9*, 8224-8236.
- (6) Song, Y.; Chen, Y.; Li, P.; Dong, C.-M. Photoresponsive Polypeptide-Glycosylated Dendron Amphiphiles: UV-Triggered Polymersomes, OVA Release, and In Vitro Enhanced Uptake and Immune Response. *Biomacromolecules* **2020**, *21*, 5345-5357.
- (7) Dunbar Cynthia, E.; High Katherine, A.; Joung, J. K.; Kohn Donald, B.; Ozawa, K.; Sadelain, M. Gene Therapy Comes of Age. *Science* **2018**, *359*, eaan4672.
- (8) Wahane, A.; Waghmode, A.; Kappahn, A.; Dhuri, K.; Gupta, A.; Bahal, R. Role of Lipid-Based and Polymer-Based Non-Viral Vectors in Nucleic Acid Delivery for Next-Generation Gene Therapy. *Molecules* **2020**, *25*, 2866-2888.
- (9) Durymanov, M.; Reineke, J. Non-Viral Delivery of Nucleic Acids: Insight Into Mechanisms of Overcoming Intracellular Barriers. *Front. Pharmacol.* **2018**, *9*, 971.



- (10) Lächelt, U.; Wagner, E. Nucleic Acid Therapeutics Using Polyplexes: A Journey of 50 Years (and Beyond). *Chem. Rev.* **2015**, *115*, 11043-11078.
- (11) Bus, T.; Traeger, A.; Schubert, U. S. The Great Escape: How Cationic Polyplexes Overcome The Endosomal Barrier. *J. Mater. Chem. B* **2018**, *6*, 6904-6918.
- (12) Kou, L.; Sun, J.; Zhai, Y.; He, Z. The Endocytosis and Intracellular Fate of Nanomedicines: Implication for Rational Design. *Asian J. of Pharm.* **2013**, *8*, 1-10.
- (13) Ingle, N. P.; Hexum, J. K.; Reineke, T. M. Polyplexes Are Endocytosed by and Trafficked within Filopodia. *Biomacromolecules* **2020**, *21*, 1379-1392.
- (14) Monsigny, M.; Roche, A.-C.; Midoux, P.; Mayer, R. Glycoconjugates as Carriers for Specific Delivery of Therapeutic Drugs and Genes. *Adv. Drug Deliv. Rev.* **1994**, *14*, 1-24.
- (15) Wagner, E.; Curiel, D.; Cotten, M. Delivery of Drugs, Proteins and Genes into Cells Using Transferrin as a Ligand for Receptor-Mediated Endocytosis. *Adv. Drug Deliv. Rev.* **1994**, *14*, 113-135.
- (16) Eiríksdóttir, E.; Konate, K.; Langel, Ü.; Divita, G.; Deshayes, S. Secondary Structure of Cell-Penetrating Peptides Controls Membrane Interaction and Insertion. *Biochim. Biophys. Acta* **2010**, *1798*, 1119-1128.
- (17) Song, Z.; Fu, H.; Wang, R.; Pacheco, L. A.; Wang, X.; Lin, Y.; Cheng, J. Secondary Structures in Synthetic Polypeptides from N-carboxyanhydrides: Design, Modulation, Association, and Material Applications. *Chem. Soc. Rev.* **2018**, *47*, 7401-7425.
- (18) Koren, E.; Torchilin, V. P. Cell-Penetrating Peptides: Breaking Through to the Other Side. *Trends Mol. Med.* **2012**, *18*, 385-393.
- (19) Lee, M. W.; Han, M.; Bossa, G. V.; Snell, C.; Song, Z.; Tang, H.; Yin, L.; Cheng, J.; May, S.; Luijten, E.; Wong, G. C. L. Interactions between Membranes and “Metaphilic” Polypeptide Architectures with Diverse Side-Chain Populations. *ACS Nano* **2017**, *11*, 2858-2871.

- (20) Rajpal; Mann, A.; Khanduri, R.; Naik, R. J.; Ganguli, M. Structural Rearrangements and Chemical Modifications in Known Cell Penetrating Peptide Strongly Enhance DNA Delivery Efficiency. *J. Control. Release* **2012**, *157*, 260-271.
- (21) Gabrielson, N. P.; Lu, H.; Yin, L.; Li, D.; Wang, F.; Cheng, J. Reactive and Bioactive Cationic  $\alpha$ -Helical Polypeptide Template for Nonviral Gene Delivery. *Angew. Chem Int. Ed.* **2012**, *51*, 1143-1147.
- (22) Mann, A.; Thakur, G.; Shukla, V.; Ganguli, M. Peptides in DNA Delivery: Current Insights and Future Directions. *Drug Discov. Today* **2008**, *13*, 152-160.
- (23) González-Henríquez, C. M.; Sarabia-Vallejos, M. A.; Rodríguez-Hernández, J. Strategies to Fabricate Polypeptide-Based Structures via Ring-Opening Polymerization of N-Carboxyanhydrides. *Polymers* **2017**, *9*, 511.
- (24) Rasines Mazo, A.; Allison-Logan, S.; Karimi, F.; Chan, N. J.-A.; Qiu, W.; Duan, W.; O'Brien-Simpson, N. M.; Qiao, G. G. Ring Opening Polymerization of  $\alpha$ -Amino Acids: Advances in Synthesis, Architecture and Applications of Polypeptides and Their Hybrids. *Chem. Soc. Rev.* **2020**, *49*, 4737-4834.
- (25) Bonduelle, C.; Huang, J.; Ibarboure, E.; Heise, A.; Lecommandoux, S. Synthesis and Self-Assembly of "Tree-Like" Amphiphilic Glycopolypeptides. *Chem. Commun.* **2012**, *48*, 8353-8355.
- (26) Quadir, M. A.; Martin, M.; Hammond, P. T. Clickable Synthetic Polypeptides—Routes to New Highly Adaptive Biomaterials. *Chem. Mater.* **2014**, *26*, 461-476.
- (27) Schatz, C.; Louguet, S.; Le Meins, J.-F.; Lecommandoux, S. Polysaccharide-block-polypeptide Copolymer Vesicles: Towards Synthetic Viral Capsids. *Angew. Chem. int. Ed.* **2009**, *48*, 2572-2575.
- (28) Guo, J.; Huang, Y.; Jing, X.; Chen, X. Synthesis and Characterization of Functional Poly( $\gamma$ -Benzyl-L-Glutamate) (PBLG) as a Hydrophobic Precursor. *Polymer* **2009**, *50*, 2847-2855.

- (29) Manai, G.; Houimel, H.; Rigoulet, M.; Gillet, A.; Fazzini, P.-F.; Ibarra, A.; Balor, S.; Roblin, P.; Esvan, J.; Coppel, Y.; Chaudret, B.; Bonduelle, C.; Tricard, S. Bidimensional Lamellar Assembly by Coordination of Peptidic Homopolymers to Platinum Nanoparticles. *Nat. Commun.* **2020**, *11*, 2051-2057.
- (30) Barz, M.; Duro-Castano, A.; Vicent, M. J. A Versatile Post-Polymerization Modification Method for Polyglutamic Acid: Synthesis of Orthogonal Reactive Polyglutamates and Their Use in “Click Chemistry”. *Polym. Chem.* **2013**, *4*, 2989-2994.
- (31) Mildner, R.; Menzel, H. Facile Synthesis of pH-Responsive Glycopolypeptides with Adjustable Sugar Density. *J. Polym. Sci. A Polym. Chem.* **2013**, *51*, 3925-3931.
- (32) Krivitsky, A.; Polyak, D.; Scomparin, A.; Eliyahu, S.; Ori, A.; Avkin-Nachum, S.; Krivitsky, V.; Satchi-Fainaro, R. Structure–Function Correlation of Aminated Poly( $\alpha$ )glutamate as siRNA Nanocarriers. *Biomacromolecules* **2016**, *17*, 2787-2800.
- (33) Niño-Pariente, A.; Armiñán, A.; Reinhard, S.; Scholz, C.; Wagner, E.; Vicent, M. J. Design of Poly-L-Glutamate-Based Complexes for pDNA Delivery. *Macromol. Biosci.* **2017**, *17*, 1700029.
- (34) Callari, M.; Wong, S.; Lu, H.; Aldrich-Wright, J.; de Souza, P.; Stenzel, M. H. Drug Induced Self-Assembly of Triblock Copolymers into Polymersomes for the Synergistic Dual-Drug Delivery of Platinum Drugs and Paclitaxel. *Polym. Chem.* **2017**, *8*, 6289-6299.
- (35) Singer, J.; Baker, B.; de Vries, P.; Kumar, A.; Shaffer, S.; Vawter, E.; Bolton, M.; Garzone, P. Poly-(L)-Glutamic Acid-Paclitaxel (CT-2103) [XYOTAX], a Biodegradable Polymeric Drug Conjugate: Characterization, Preclinical Pharmacology, and Preliminary Clinical Data. *Adv. Exp. Med. Biol.* **2003**, *519*, 81-109.
- (36) Paclitaxel, Polyglutamate Paclitaxel, or Observation in Treating Patients With Stage III or Stage IV Ovarian Epithelial, Peritoneal Cancer, or Fallopian Tube Cancer. <https://clinicaltrials.gov/ct2/show/NCT00108745?term=Poly-%28L%29-glutamic+acid-paclitaxel&draw=2&rank=2#wrapper> (October 18, 2021),

- (37) Tang, H.; Yin, L.; Kim, K. H.; Cheng, J. Helical Poly(Arginine) Mimics with Superior Cell-Penetrating and Molecular Transporting Properties. *Chem. Sci.* **2013**, *4*, 3839-3844.
- (38) Gabrielson, N. P.; Lu, H.; Yin, L.; Li, D.; Wang, F.; Cheng, J. Reactive and Bioactive Cationic  $\alpha$ -Helical Polypeptide Template for Nonviral Gene Delivery. **2012**, *51*, 1143-1147.
- (39) Ge, C.; Yang, J.; Duan, S.; Liu, Y.; Meng, F.; Yin, L. Fluorinated  $\alpha$ -Helical Polypeptides Synchronize Mucus Permeation and Cell Penetration toward Highly Efficient Pulmonary siRNA Delivery against Acute Lung Injury. *Nano Letters* **2020**, *20*, 1738-1746.
- (40) Liu, B.; Zhang, Q.; Zhou, F.; Ren, L.; Zhao, Y.; Yuan, X. Enhancing Membrane-Disruptive Activity via Hydrophobic Phenylalanine and Lysine Tethered to Poly(Aspartic Acid). *ACS Appl. Mater. Interfaces* **2019**, *11*, 14538-14547.
- (41) Yu, Z.; Zhang, Z.; Yan, J.; Zhao, Z.; Ge, C.; Song, Z.; Yin, L.; Tang, H. Guanidine-Rich Helical Polypeptides Bearing Hydrophobic Amino Acid Pendants for Efficient Gene Delivery. *Biomater. Sci.* **2021**, *9*, 2670-2678.
- (42) Conejos-Sánchez, I.; Duro-Castano, A.; Birke, A.; Barz, M.; Vicent, M. J. A Controlled and Versatile NCA Polymerization Method for the Synthesis of Polypeptides. *Polym. Chem.* **2013**, *4*, 3182-3186.
- (43) Schneider, C. A.; Rasband, W. S.; Eliceiri, K. W. NIH Image to ImageJ: 25 Years of Image Analysis. *Nat. methods* **2012**, *9*, 671-675.
- (44) Richter, F.; Mapfumo, P.; Martin, L.; Solomun, J. I.; Hausig, F.; Frietsch, J. J.; Ernst, T.; Hoepfener, S.; Brendel, J. C.; Traeger, A. Improved Gene Delivery to K-562 Leukemia Cells by Lipoic Acid Modified Block Copolymer Micelles. *J. Nanobiotechnology* **2021**, *19*, 70-84.
- (45) Richter, F.; Leer, K.; Martin, L.; Mapfumo, P.; Solomun, J. I.; Kuchenbrod, M. T.; Hoepfener, S.; Brendel, J. C.; Traeger, A. The Impact of Anionic Polymers on Gene Delivery: How Composition and Assembly Help Evading the Toxicity-Efficiency Dilemma. *J. Nanobiotechnology* **2021**, *19*, 292-306.

- (46) Schindelin, J.; Arganda-Carreras, I.; Frise, E.; Kaynig, V.; Longair, M.; Pietzsch, T.; Preibisch, S.; Rueden, C.; Saalfeld, S.; Schmid, B.; Tinevez, J.-Y.; White, D. J.; Hartenstein, V.; Eliceiri, K.; Tomancak, P.; Cardona, A. Fiji: An Open-Source Platform for Biological-Image Analysis. *Nat. methods* **2012**, *9*, 676-682.
- (47) Aescht, E.; Büchl-Zimmermann, S.; Burmester, A.; Dänhardt-Pfeiffer, S.; Desel, C.; Hamers, C.; Jach, G.; Kässens, M.; Makovitzky, J.; Mulisch, M.; Nixdorf-Bergweiler, B.; Pütz, D.; Riedelsheimer, B.; Boom, F.; Wegerhoff, R.; Welsch, U., *Romeis - Mikroskopische Technik*. 18 ed.; Springer-Verlag: Heidelberg, 2010.
- (48) Bonduelle, C. Secondary Structures of Synthetic Polypeptide Polymers. *Polym. Chem.* **2018**, *9*, 1517-1529.
- (49) Huesmann, D.; Birke, A.; Klinker, K.; Türk, S.; Räder, H. J.; Barz, M. Revisiting Secondary Structures in NCA Polymerization: Influences on the Analysis of Protected Polylysines. *Macromolecules* **2014**, *47*, 928-936.
- (50) Miyazawa, T.; Blout, E. R. The Infrared Spectra of Polypeptides in Various Conformations: Amide I and II Bands. *J. Am. Chem. Soc.* **1961**, *83*, 712-719.
- (51) Bonduelle, C.; Makni, F.; Severac, L.; Piedra-Arroni, E.; Serpentine, C.-L.; Lecommandoux, S.; Pratviel, G. Smart Metallopoly(L-Glutamic Acid) Polymers: Reversible Helix-to-Coil Transition at Neutral pH. *RSC Adv.* **2016**, *6*, 84694-84697.
- (52) Eltoukhy, A. A.; Chen, D.; Alabi, C. A.; Langer, R.; Anderson, D. G. Degradable Terpolymers with Alkyl Side Chains Demonstrate Enhanced Gene Delivery Potency and Nanoparticle Stability. *Adv. Mater.* **2013**, *25*, 1487-1493.
- (53) Nelson, C. E.; Kintzing, J. R.; Hanna, A.; Shannon, J. M.; Gupta, M. K.; Duvall, C. L. Balancing Cationic and Hydrophobic Content of PEGylated siRNA Polyplexes Enhances Endosome Escape, Stability, Blood Circulation Time, and Bioactivity In Vivo. *ACS Nano* **2013**, *7*, 8870-8880.

- (54) Rémy-Kristensen, A.; Clamme, J.-P.; Vuilleumier, C.; Kuhry, J.-G.; Mély, Y. Role of endocytosis in the transfection of L929 fibroblasts by polyethylenimine/DNA complexes. *Biochim. Biophys. Acta Biomembr.* **2001**, *1514*, 21-32.
- (55) Hertz, D.; Leiske, M. N.; Wloka, T.; Traeger, A.; Hartlieb, M.; Kessels, M. M.; Schubert, S.; Qualmann, B.; Schubert, U. S. Comparison of random and gradient amino functionalized poly(2-oxazoline)s: Can the transfection efficiency be tuned by the macromolecular structure? *J. Polym. Sci. A Polym. Chem.* **2018**, *56*, 1210-1224.
- (56) Monnery, B. D.; Wright, M.; Cavill, R.; Hoogenboom, R.; Shaunak, S.; Steinke, J. H. G.; Thanou, M. Cytotoxicity of Polycations: Relationship of Molecular Weight and the Hydrolytic Theory of the Mechanism of Toxicity. *Int. J. Pharm.* **2017**, *521*, 249-258.
- (57) Liu, Z.; Zhang, Z.; Zhou, C.; Jiao, Y. Hydrophobic Modifications of Cationic polymers for Gene Delivery. *Prog. Polym. Sci.* **2010**, *35*, 1144-1162.
- (58) Zhang, R.; Zheng, N.; Song, Z.; Yin, L.; Cheng, J. The effect of side-chain functionality and hydrophobicity on the gene delivery capabilities of cationic helical polypeptides. *Biomaterials* **2014**, *35*, 3443-3454.
- (59) Fang, H.; Guo, Z.; Lin, L.; Chen, J.; Sun, P.; Wu, J.; Xu, C.; Tian, H.; Chen, X. Molecular Strings Significantly Improved the Gene Transfection Efficiency of Polycations. *J. Am. Chem. Soc.* **2018**, *140*, 11992-12000.
- (60) Huotari, J.; Helenius, A. Endosome Maturation. *EMBO J.* **2011**, *30*, 3481-3500.
- (61) Incani, V.; Lavasanifar, A.; Uludağ, H. Lipid and Hydrophobic Modification of Cationic Carriers on Route to Superior Gene Vectors. *Soft Matter* **2010**, *6*, 2124-2138.
- (62) Rejman, J.; Oberle, V.; Zuhorn, I. S.; Hoekstra, D. Size-Dependent Internalization of Particles via The Pathways of Clathrin- and Caveolae-Mediated Endocytosis. *Biochem. J.* **2004**, *377*, 159-169.
- (63) Shang, L.; Nienhaus, K.; Nienhaus, G. U. Engineered Nanoparticles Interacting with Cells: Size Matters. *J. Nanobiotechnology* **2014**, *12*, 5-15.

- (64) Tan, Z.; Jiang, Y.; Zhang, W.; Karls, L.; Lodge, T. P.; Reineke, T. M. Polycation Architecture and Assembly Direct Successful Gene Delivery: Micelleplexes Outperform Polyplexes via Optimal DNA Packaging. *J. Am. Chem. Soc.* **2019**, *141*, 15804-15817.
- (65) González-Domínguez, I.; Puente-Massaguer, E.; Lavado-García, J.; Cervera, L.; Gòdia, F. Micrometric DNA/PEI polyplexes correlate with higher transient gene expression yields in HEK 293 cells. *N. Biotechnol.* **2022**, *68*, 87-96.
- (66) Solomun, J. I.; Cinar, G.; Mapfumo, P.; Richter, F.; Moek, E.; Hausig, F.; Martin, L.; Hoepfener, S.; Nischang, I.; Traeger, A. Solely Aqueous Formulation of Hydrophobic Cationic Polymers for Efficient Gene Delivery. *Int. J. Pharm.* **2021**, *593*, 120080.
- (67) Fröhlich, E. The role of surface charge in cellular uptake and cytotoxicity of medical nanoparticles. *Int. J. Nanomedicine* **2012**, *7*, 5577-91.
- (68) Chen, J.; Wang, K.; Wu, J.; Tian, H.; Chen, X. Polycations for Gene Delivery: Dilemmas and Solutions. *Bioconjugate Chem.* **2019**, *30*, 338-349.
- (69) Thermo Fisher Scientific, Fluorescence SpectraViewer YOYO-1. [https://www.thermofisher.com/order/fluorescence-spectraviewer?SID=srch-svtool&UID=SVgfnDNA\\_2#!/](https://www.thermofisher.com/order/fluorescence-spectraviewer?SID=srch-svtool&UID=SVgfnDNA_2#!/) (October 4, 2021),
- (70) Rehman, Z. u.; Sjollema, K. A.; Kuipers, J.; Hoekstra, D.; Zuhorn, I. S. Nonviral Gene Delivery Vectors Use Syndecan-Dependent Transport Mechanisms in Filopodia To Reach the Cell Surface. *ACS Nano* **2012**, *6*, 7521-7532.
- (71) Kohler, F.; Rohrbach, A. Surfing along Filopodia: A Particle Transport Revealed by Molecular-Scale Fluctuation Analyses. *Biophys. J.* **2015**, *108*, 2114-2125.
- (72) Rehman, Z.; Zuhorn, I. S.; Hoekstra, D. How cationic lipids transfer nucleic acids into cells and across cellular membranes: recent advances. *J. Control. Release* **2013**, *166*, 46-56.
- (73) Lehmann, M. J.; Sherer, N. M.; Marks, C. B.; Pypaert, M.; Mothes, W. Actin- and myosin-driven movement of viruses along filopodia precedes their entry into cells. *J. Cell Biol.* **2005**, *170*, 317-325.

- (74) Rejman, J.; Conese, M.; Hoekstra, D. Gene transfer by means of lipo- and polyplexes: role of clathrin and caveolae-mediated endocytosis. *J. Liposome Res.* **2006**, *16*, 237-47.
- (75) Mayor, S.; Pagano, R. E. Pathways of clathrin-independent endocytosis. *Nat. Rev. Mol. Cell Biol.* **2007**, *8*, 603-612.
- (76) ur Rehman, Z.; Sjollema, K. A.; Kuipers, J.; Hoekstra, D.; Zuhorn, I. S. Nonviral gene delivery vectors use syndecan-dependent transport mechanisms in filopodia to reach the cell surface. *ACS Nano* **2012**, *6*, 7521-7532.
- (77) Reifarth, M.; Hoepfner, S.; Schubert, U. S. Uptake and Intracellular Fate of Engineered Nanoparticles in Mammalian Cells: Capabilities and Limitations of Transmission Electron Microscopy—Polymer-Based Nanoparticles. *Adv. Mater.* **2018**, *30*, 1703704.
- (78) Gilleron, J.; Querbes, W.; Zeigerer, A.; Borodovsky, A.; Marsico, G.; Schubert, U.; Manygoats, K.; Seifert, S.; Andree, C.; Stöter, M.; Epstein-Barash, H.; Zhang, L.; Kotliansky, V.; Fitzgerald, K.; Fava, E.; Bickle, M.; Kalaidzidis, Y.; Akinc, A.; Maier, M.; Zerial, M. Image-Based Analysis of Lipid Nanoparticle-Mediated siRNA Delivery, Intracellular Trafficking and Endosomal Escape. *Nat. Biotechnol.* **2013**, *31*, 638-646.
- (79) Doherty, G. J.; McMahon, H. T. Mechanisms of Endocytosis. *Annu. Rev. Biochem.* **2009**, *78*, 857-902.
- (80) Smith, S. A.; Selby, L. I.; Johnston, A. P. R.; Such, G. K. The Endosomal Escape of Nanoparticles: Toward More Efficient Cellular Delivery. *Bioconjugate Chem.* **2019**, *30*, 263-272.